

# Antithetic Noise in Diffusion Models

Jing Jia<sup>1</sup>, Sifan Liu<sup>\*2</sup>, Bowen Song<sup>3</sup>, Wei Yuan<sup>4</sup>, Liyue Shen<sup>\*3</sup>, and  
Guanyang Wang<sup>\*4</sup>

<sup>1</sup>Department of Computer Science, Rutgers University,

`jing.jia@rutgers.edu`

<sup>2</sup>Flatiron Institute,

`sliu@flatironinstitute.org`

<sup>3</sup>Department of EECS, University of Michigan,

`{bowenbw, liyues}@umich.edu`

<sup>4</sup>Department of Statistics, Rutgers University,

`{wy204, guanyang.wang}@rutgers.edu`

June 13, 2025

## Abstract

We initiate a systematic study of antithetic initial noise in diffusion models. Across unconditional models trained on diverse datasets, text-conditioned latent-diffusion models, and diffusion posterior samplers, we find that pairing each initial noise with its negation consistently yields strongly negatively correlated samples. To explain this phenomenon, we combine experiments and theoretical analysis, leading to a *symmetry conjecture* that the learned score function is approximately affine antisymmetric (odd symmetry up to a constant shift), and provide evidence supporting it. Leveraging this negative correlation, we enable two applications: (1) enhancing image diversity in models like Stable Diffusion without quality loss, and (2) sharpening uncertainty quantification (e.g., up to 90% narrower confidence intervals) when estimating downstream statistics. Building on these gains, we extend the two-point pairing to a randomized quasi-Monte Carlo estimator, which further improves estimation accuracy. Our framework is training-free, model-agnostic, and adds no runtime overhead.

---

\*Co-corresponding authors

# Contents

<b>1</b>	<b>Introduction</b>	<b>3</b>
<b>2</b>	<b>Setup and motivation</b>	<b>5</b>
2.1	Motivation . . . . .	6
<b>3</b>	<b>Negative correlation from antithetic noise</b>	<b>7</b>
3.1	Pixel-wise correlations: antithetic vs. independent noise . . . . .	7
3.2	Explanatory experiments: temporal correlations & symmetry conjecture .	8
3.3	An alternative explanation via the FKG inequality . . . . .	11
<b>4</b>	<b>Uncertainty quantification</b>	<b>11</b>
<b>5</b>	<b>Experiments</b>	<b>14</b>
5.1	Improving diversity . . . . .	14
5.2	Uncertainty quantification . . . . .	15
5.2.1	Estimating pixel-wise statistics . . . . .	15
5.2.2	Estimating reconstruction uncertainty in Bayesian inverse problems	16
<b>6</b>	<b>Potential, limitations, and future directions</b>	<b>17</b>
<b>A</b>	<b>Proofs</b>	<b>24</b>
A.1	Proofs in Section 3.2 . . . . .	24
A.2	Proofs in Section 3.3 . . . . .	24
A.3	Proofs in Section 4 . . . . .	25
A.3.1	Monte Carlo estimator: . . . . .	25
A.3.2	Antithetic Monte Carlo Estimator: . . . . .	26
<b>B</b>	<b>Additional Experiments</b>	<b>27</b>
B.1	Additional experiments on Pixel-Wise Correlations . . . . .	27
B.1.1	DDPM . . . . .	27
B.1.2	DPS . . . . .	29
B.2	Additional experiments on the symmetry conjecture . . . . .	30
B.3	Additional experiments for uncertainty quantification . . . . .	36
B.3.1	Uncertainty Quantification . . . . .	36
B.3.2	QMC Experiments . . . . .	37
B.3.3	DPS Experiment . . . . .	38
<b>C</b>	<b>More visualizations</b>	<b>40</b>

# 1 Introduction

Diffusion models have set the state of the art in photorealistic image synthesis, high-fidelity audio, and video generation [45, 12, 51, 18]; they also power applications such as text-to-image generation [40], image editing and restoration [31], and inverse problem solving [50].

For many pretrained diffusion models, sampling relies on three elements: the network weights, the denoising schedule, and the initial Gaussian noise. Once these are fixed, sampling is often deterministic: the sampler transforms the initial noise into an image via successive denoising passes.

Much of the literature improves the first two ingredients and clusters into two strands: (i) architectural and training developments, which improve sample quality and scalability through backbone or objective redesign (e.g., EDM [15], Latent Diffusion Models [40], DiT [37]), and (ii) accelerated sampling, which reduces the number of denoising steps while retaining high-quality generation (e.g., DDIM [48], Consistency Models [49], DPM-Solver++ [26], and progressive distillation [43]).

However, the third ingredient—the *initial Gaussian noise*—has received comparatively little attention. Previous work examines it mostly through task-specific lenses: InitNO [11] separates Gaussian noise seeds into “valid” and “invalid” groups according to their attention-score profiles. Qi et al. [39] show that inversion-stable noises reliably boost the quality of generated images. Zhou et al. [63] propose a learning framework to select high quality noises. The Crystal Ball detector [2] pinpoints “trigger patches” as crucial elements in object synthesis. FIND [5] optimizes the initial noise distribution so that outputs better match user prompts. CCS [47] exploits an almost linear noise-to-image mapping to achieve controllable generation. Nevertheless, a systematic analysis of how the initial noise itself shapes the final outputs is still missing.

Our perspective is orthogonal to prior work. Our first contribution is a *simple yet model-agnostic finding*: across unconditional, latent text-conditioned, and posterior-sampling diffusion models, pairing every Gaussian noise  $z$  with its negation  $-z$ —known as *antithetic sampling* [36]—consistently produces samples that are **strongly negatively correlated**. This phenomenon is *universal* as it holds regardless of architecture, dataset, sampling schedule, and both conditional and unconditional sampling. To illuminate this phenomenon, we conduct explanatory experiments and theoretical analysis, conjecture that the learned score function exhibits approximate affine symmetry, and present initial supporting evidence.

Leveraging this universal property, we present two concrete applications:

(i) **Enhanced image diversity**. As shown in Figure 1, negative correlation implies

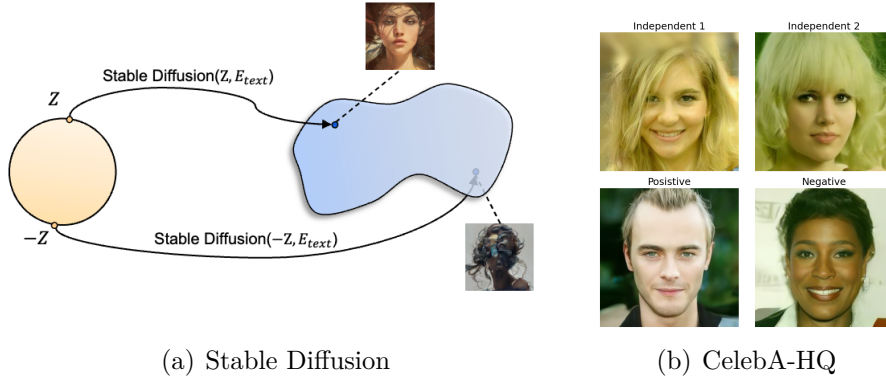


Figure 1: Antithetic noise produces visually “opposite” images. Left: a Stable Diffusion sketch with the prompt “cover, hyperdetailed painting, luminism, Bar lighting, complex, head and shoulders portrait.” Right: images from independent random-noise pairs (top) vs. an antithetic pair (bottom).

diversity. Because each antithetic noise pair drives the reverse-diffusion trajectories toward distant regions of the data manifold, the paired-sampling scheme markedly increases diversity “for free” compared with independent noise inputs, while still maintaining high image quality. The procedure is fully *plug-and-play*: one simply feeds the model with antithetic noise vectors.

**(ii) Sharper uncertainty quantification.** Because each antithetic pair generates strongly negatively correlated samples, these outputs form an effective control-variate pair. We apply this idea in an antithetic estimator for downstream statistics, reducing the 95% confidence-interval width by up to 90% and cutting computational effort by about 100 times compared to standard Monte Carlo sampling with independent noise.

Building on the variance gains from antithetic pairs, we generalize the idea to apply quasi-Monte Carlo (QMC) and randomized QMC (RQMC). The resulting RQMC estimator often delivers further variance reduction. Although QMC has been widely used in computer graphics [16, 54], quantitative finance [14, 28], and Bayesian inference [4, 23], this is, to our knowledge, its first application to diffusion models.

Together, these results suggest that principled manipulations in the initial-noise space can be a promising avenue for further gains in diffusion model’s efficiency, output diversity, and reliability.

The remainder of the paper is organized as follows. Section 2 defines the problem and outlines our motivation. Section 3 presents our central finding that antithetic noise pairs produce strongly negatively correlated outputs. We offer both theoretical and empirical explanations for this phenomenon, and present the *symmetry conjecture* in Section 3.2. Section 4 details the construction of point estimates and confidence intervals using antithetic sampling for estimating downstream statistics, illustrates how antithetic

sampling tightens confidence bounds, and discusses the generalization to QMC. Section 5 reports experiments on the aforementioned applications. Finally, Section 6 discusses our method’s potentials, limitations, and future directions. Appendix A, B, and C include proofs, additional experiments and detailed setups, and supplemental visualizations, respectively.

## 2 Setup and motivation

**Unconditional diffusion model:** A diffusion model aims to generate samples from an unknown data distribution  $p_0$ . It first *noises* data towards a standard Gaussian by applying progressively stronger Gaussian perturbations, then learns to reverse the process so that pure white noise can be *denoised* step-by-step back into target samples. The forward process simulates a stochastic differential equation (SDE):  $d\mathbf{x}_t = \mu(\mathbf{x}_t, t)dt + \sigma_t d\mathbf{w}_t$ , where  $\{\mathbf{w}_t\}_{t=0}^T$  denotes the standard Brownian motion, and  $\mu(\mathbf{x}, t), \sigma_t$  are chosen by the users. Let  $p_t$  denote the distribution of  $\mathbf{x}_t$ , where  $\mathbf{x}_0 \sim p_0$ . A key result in [51] states that if we sample  $\mathbf{y}_T \sim p_T$  and simulate the probability-flow ordinary differential equation (PF-ODE) backward from time  $T$  to 0 as

$$d\mathbf{y}_t = \left( -\mu(\mathbf{y}_t, t) - \frac{1}{2}\sigma_t^2 \nabla \log p(\mathbf{y}_t, t) \right) dt, \quad (1)$$

then for every time  $t$  the marginal distribution of  $\mathbf{y}_t$  coincides with  $p_t$ . Thus in an idealized world, one can perfectly sample from  $p_0$  by simulating the PF-ODE (1).

In practice, the score function  $\nabla \log p_t(\mathbf{x}, t)$  is unavailable, and a neural network  $\epsilon_\theta^{(t)}(\mathbf{x})$  is trained to approximate it, where  $\theta$  represents its weights. The drift term  $\mu$  and diffusion term  $\sigma$  are designed such that  $p_t$  converges to a standard Gaussian as  $t \rightarrow \infty$ . Therefore, one can generate new samples from  $p_0$  by first sampling a Gaussian noise and simulating the PF-ODE (1) through some numerical integrator from  $T$  to 0. For example, DDIM [48] has the (discretized) forward process as  $\mathbf{x}_k | \mathbf{x}_{k-1} \sim \mathbb{N}(\sqrt{\alpha_k}\mathbf{x}_{k-1}, (1 - \alpha_k)I)$  for  $k = 0, 1, \dots, T - 1$ , and backward sampling process as

$$\mathbf{y}_T \sim \mathbb{N}(0, I), \quad \mathbf{y}_{t-1} = \sqrt{\alpha_{t-1}} \left( \frac{\mathbf{y}_t - \sqrt{1 - \alpha_t} \epsilon_\theta^{(t)}(\mathbf{y}_t)}{\sqrt{\alpha_t}} \right) + \sqrt{1 - \alpha_{t-1}} \epsilon_\theta^{(t)}(\mathbf{y}_t). \quad (2)$$

Once  $\theta$  is fixed, the randomness in DDIM sampling comes solely from the initial Gaussian noise.

We remark that samples from  $p_0$  can also be drawn by simulating the backward SDE with randomness at each step, as in the DDPM sampler [12, 51]. Throughout the main text, we focus on deterministic samplers such as DDIM to explain our idea. In Appendix

B, we present additional experiments showing that our findings also extend to stochastic samplers like DDPM.

**Text-conditioned latent diffusion:** In Stable Diffusion and its successors SDXL [38] and SDXL Turbo [44], a pretrained VAE first compresses each image to a latent tensor  $z \in \mathcal{Z}$ . A frozen text encoder embeds the prompt as  $c \in \mathbb{R}^m$ . During training, the network  $\epsilon_\theta^{(t)}$  receives  $(z_t, c)$  and learns  $\nabla_{z_t} \log p_t(z_t | c)$ . At generation time we draw latent noise  $z_T \sim \mathbb{N}(0, I)$  and run the reverse diffusion from  $t = T$  to 0, yielding a denoised latent  $z_0$ , which the decoder maps back to pixels. Thus, given a prompt  $c$  and an initial Gaussian noise, the sampler produces an image from  $p_0(\cdot | c)$ .

**Diffusion posterior sampling:** Diffusion model has also been utilized as a prior for posterior sampling in many inverse problems. Suppose we observe only a partial or corrupted measurement  $\mathbf{y}_{\text{obs}} = \mathcal{A}(\mathbf{x}) + \text{noise}$  from an unknown signal  $\mathbf{x}$  via a known forward operator  $\mathcal{A}$ . From a Bayesian perspective, we impose a prior  $p(\mathbf{x})$  on  $\mathbf{x}$ , and perform inference based on the posterior  $p(\mathbf{x} | \mathbf{y}_{\text{obs}}) \propto p(\mathbf{y}_{\text{obs}} | \mathbf{x}) p(\mathbf{x})$ . Diffusion posterior sampling arises when  $p(\mathbf{x})$  is given by a pretrained diffusion model. Given initial noise  $z$  and observed  $\mathbf{y}_{\text{obs}}$ , diffusion posterior samplers apply a sequence of denoising steps from  $T$  to 0, each step resembling (2) but incorporating  $\mathbf{y}_{\text{obs}}$  [7, 50, 46].

## 2.1 Motivation

Beyond examining how variations in the initial noise affect the outputs, several technical considerations motivate our focus on the antithetic noise pair  $(z, -z)$  for diffusion models. Let DM denote certain diffusion model’s mapping from an initial noise vector to a generated sample.

- **Preserving quality:** Since  $z \sim \mathbb{N}(0, I)$  implies  $-z \sim \mathbb{N}(0, I)$ , the initial noises  $z$  and  $-z$  share the same marginal distribution. Consequently,  $\text{DM}(z) \stackrel{d}{=} \text{DM}(-z)$ , so all per-sample statistics remain unchanged. In other words, negating the initial noise does not degrade generation quality.
- **Maximal separation in the noise space:** High-dimensional Gaussians concentrate on the sphere of radius  $\sqrt{\text{dimension}}$  [52], so any draw  $z$  and its negation  $-z$  lie at opposite poles of that hypersphere. This antipodal pairing represents the maximum possible perturbation in noise space, making it a natural extreme test of the sampler’s behavior.
- **Measuring (non-)linearity:** Recent work has examined how closely score networks approximate linear operators. Empirical studies across various diffusion settings show

that these networks behave as locally linear maps; this behavior forms the basis for new controllable sampling schemes [6, 21, 47]. Since linear transformations preserve correlation, we can use correlation to evaluate linearity: if a score network were exactly linear, feeding it with noises  $z$  and  $-z$  would yield a correlation of  $-1$  between  $\text{DM}(z)$  and  $\text{DM}(-z)$ . Thus, the difference between the observed correlation and  $-1$  provides a direct measure of the network’s departure from linearity.

### 3 Negative correlation from antithetic noise

#### 3.1 Pixel-wise correlations: antithetic vs. independent noise

Table 1 reports Pearson correlations between pixel values of image pairs produced by pretrained DDIM models under two noise schemes—PN (positive vs. negative:  $z$  vs.  $-z$ ) and RR (random vs. random:  $z_1$  vs.  $z_2$ )—across CIFAR-10 [19], CelebA-HQ [58], Church [61], and Stable Diffusion.

- CIFAR-10, CelebA-HQ, Church: For each of these three datasets, we draw 1600 antithetic noise pairs, compute the pixelwise correlation for each generated image pair, and report their average. We repeat the same procedure with 1600 independent random noise pairs for comparison.
- Stable Diffusion: Since this is a prompt-based model, we use two common benchmarks (DrawBench and Pick-a-Pic) and randomly select 100 prompts from each. For each prompt, we generate 100 antithetic and 100 independent noise pairs, measuring and averaging the resulting correlations.

Across all datasets, PN pairs have markedly and consistently lower pixel correlations than RR pairs. Their average correlation never surpasses  $-0.33$  and can dip below  $-0.7$ . In contrast, RR pairs show mildly positive correlations, reflecting the consistent overall outlines enforced by the model’s architecture and training dataset. Moreover, the 75% quantile of PN correlation is frequently even lower than the lowest RR correlation. The histogram of pixel-wise correlation coefficients is plotted in Figure 2. The PN pair correlations are heavily left-skewed—most coefficients range from  $-0.9$  to  $-0.4$ —whereas the RR correlations span a broader, nearly symmetric range centered just above zero.

The same behavior appears in both DDPM models and diffusion posterior samplers, which we report in Appendix B.1. These results demonstrate that the negative correlation resulted from antithetic sampling is a universal phenomenon across various datasets and diffusion models.

Table 1: Pearson correlation coefficients for PN and RR pairs.

Statistic	CIFAR10		CelebA		Church		Stable Diffusion	
	PN	RR	PN	RR	PN	RR	PN	RR
Mean	-0.76	0.05	-0.33	0.24	-0.62	0.08	-0.47	0.05
Min	-0.97	-0.68	-0.87	-0.66	-0.95	-0.46	-0.71	-0.23
25th percentile	-0.85	-0.11	-0.47	0.12	-0.70	-0.04	-0.54	-0.02
75th percentile	-0.71	0.21	-0.22	0.39	-0.55	0.19	-0.40	0.11
Max	0.08	0.74	0.49	0.78	-0.21	0.67	-0.18	0.33

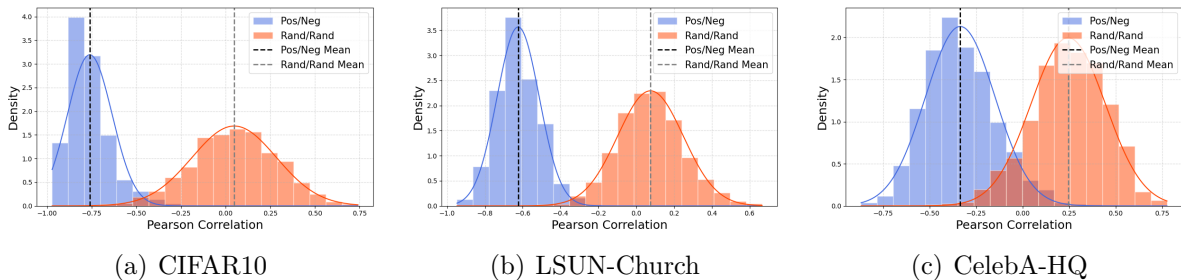


Figure 2: Pearson Correlation histograms for PN and RR pairs across three datasets using DDIM. Dashed lines indicate the average Pearson correlation for each group.

### 3.2 Explanatory experiments: temporal correlations & symmetry conjecture

We aim to explain the strong negative correlation between  $DM(Z)$  and  $DM(-Z)$  for  $Z \sim \mathcal{N}(0, I)$ . Because DM performs iterative denoising through the score network  $\epsilon_\theta^{(t)}$  (see (2)), we visualize how these correlations evolve over diffusion time-steps in Figure 3.

Throughout the transition from noises to samples, the PN correlation of  $\epsilon_\theta^{(t)}$ —indicated by the orange, blue, and green dashed lines in Figure 3—starts at  $-1$ , stays strongly negative, and only climbs slightly in the final steps. This nearly  $-1$  correlation is remarkable, as it suggests that the score network  $\epsilon_\theta$  learns an approximately affine antisymmetric function. To explain, we first state the following results which shows  $-1$  correlation is equivalent to affine antisymmetric, with proof in Appendix A.1.

**Lemma 1.** *Let  $Z \sim \mathcal{N}(0, I_d)$ , suppose a map  $f : \mathbb{R}^d \rightarrow \mathbb{R}$  satisfies  $\text{Corr}(f(Z), f(-Z)) = -1$ , then  $f$  must be affine antisymmetric at  $(0, c)$  for some  $c$ , i.e.,  $f(\mathbf{x}) + f(-\mathbf{x}) = 2c$  for every  $\mathbf{x}$ .*

Lemma 1 and Figure 3 lead us to the following conjecture:

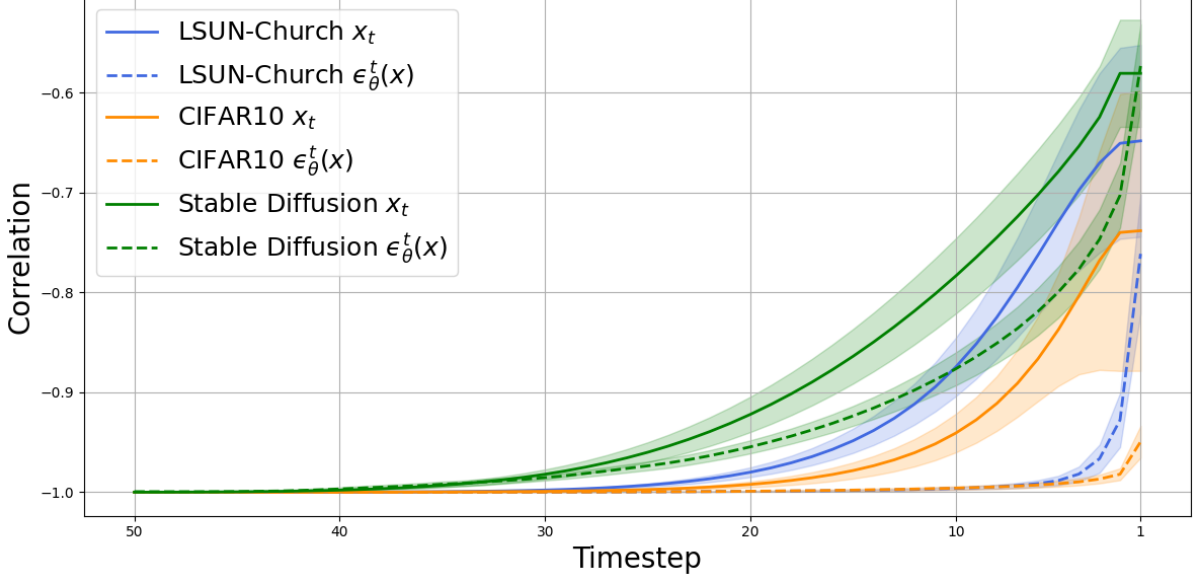


Figure 3: Correlation of  $x_t$  (solid) and  $\epsilon_\theta^{(t)}$  (dash) between antithetic (PN) pairs. Step 50 is the initial noise and Step 0 is the generated image. Shaded bands show  $\pm 1$  std. dev.

**Conjecture** For each time step  $t$ , the score network  $\epsilon_\theta^{(t)}$  is approximately affine antisymmetric at  $(\mathbf{0}, \mathbf{c}_t)$ , i.e.,

$$\epsilon_\theta^{(t)}(\mathbf{x}) + \epsilon_\theta^{(t)}(-\mathbf{x}) \approx 2\mathbf{c}_t$$

for some fixed vector  $\mathbf{c}_t$  that depends on  $t$ .

The conjecture implies that the score network has learned an “almost odd” function up to an additive shift. This is consistent with both theory and observations for large  $t$ , where  $p_t(\mathbf{x})$  is close to standard Gaussian, thus the score function is almost linear in  $\mathbf{x}$ . Nonetheless, our findings illustrate that this conjecture is far more general: it applies to every timestep  $t$  and can accommodate genuinely nonlinear odd behaviors (for example, functions like  $\sin x$ ).

This conjecture combined with the DDIM update rule (2) immediately explains the negative correlation: The one step iteration of  $F_t$  in (2) can be written as a linear combination between  $\mathbf{x}$  and the output of the score network:  $F_t(\mathbf{x}) = a_t\mathbf{x} + b_t\epsilon_\theta^{(t)}(\mathbf{x})$ . Given the conjecture,  $F_t(-\mathbf{x}) \approx -a_t\mathbf{x} - b_t\epsilon_\theta^{(t)}(\mathbf{x}) + 2b_t\mathbf{c}_t = -F_t(\mathbf{x}) + 2b_t\mathbf{c}_t$ , so the one-step DDIM update is affine antisymmetric at  $(\mathbf{0}, b_t\mathbf{c}_t)$ . Thus, beginning with a strongly negatively correlated pair, each DDIM update preserves that strong negative correlation all the way through to the final output.

To (partly) validate our conjecture, we perform the following experiment. Using a pretrained CIFAR-10 score network with a 50-step DDIM sampler, we picked time steps

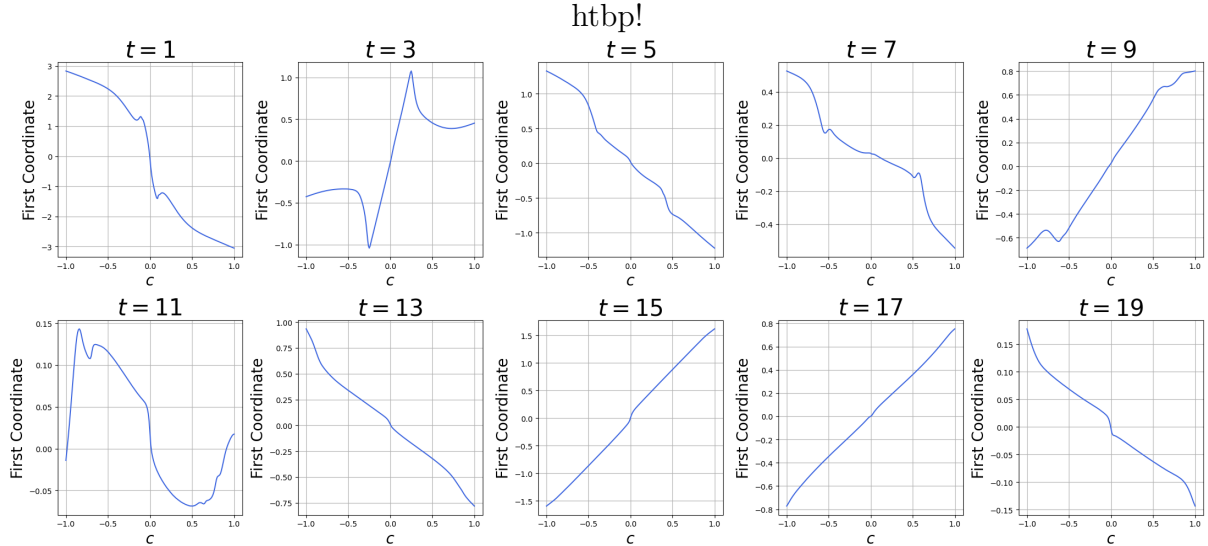


Figure 4: First-coordinate output of the pretrained score network on CIFAR10 as a function of the interpolation scalar  $c$  for a 50-step DDIM at  $t = 1, 3, \dots, 19$ .

$t = 1, 3, \dots, 19$  (where smaller  $t$  is closer to the image and larger  $t$  is closer to pure noise). For each  $t$ , we sample  $\mathbf{x} \sim \mathbb{N}(0, I_d)$ , evaluated the first coordinate of  $\epsilon_{\theta}^{(t)}(c\mathbf{x})$  as  $c$  varied from  $-1$  to  $1$  (interpolating from  $-\mathbf{x}$  to  $\mathbf{x}$ ), and plotted the result in Figure 4. We exclude  $t \geq 20$ , where the curve is very close to a straight line.

Figure 4 confirms that, at every step  $t$ , the first coordinate of the score network is indeed overall affine antisymmetric. Although the curves display nonlinear oscillations at small  $t$ , the deviations on either side are approximately mirror images, and for larger  $t$  the mapping is almost a straight line. The symmetry center  $c_t$  usually lies near zero, but not always—for instance, at  $t = 11$ ,  $c_t \approx 0.05$  even though the function spans from  $-0.05$  to  $0.15$ . Additional validation experiments—using different coordinates and alternative datasets—are presented in the Appendix B.2. Despite the distinct function shapes across coordinates, the conjectured symmetry still persists.

Both the conjecture and its empirical support could be of independent interest. They imply that the score network learns a function with strong symmetry, even though that symmetry is not explicitly enforced. The conjecture matches the Gaussian linear score approximation in the high-noise regime, which has proven effective [55]. In the intermediate-to-low noise regime, a single Gaussian approximation performs poorly—this is clear in Figure 4 for  $t = 3, 7, 11$ , where the score is strongly nonlinear—yet our conjectured approximate symmetry still holds. We believe this result provides valuable insights into pretrained score networks, which are commonly perceived as black boxes.

This experiment is mainly intended to explain our negative correlation finding and should be seen as initial evidence for the conjecture. Fully validating or disproving the symmetry conjecture would require much more extensive experiments, which we leave as

future work.

### 3.3 An alternative explanation via the FKG inequality

Consider the univariate case where a scalar Gaussian  $z$  is fed through a sequence of one-dimensional linear maps and ReLU activations. Let  $F$  be the resulting composite function. One can show that, regardless of the number of layers or the linear coefficients used,  $\text{Corr}(F(z), F(-z)) \leq 0$ . The proof (given in Appendix A.2) relies on the univariate FKG inequality [10], a well-known result in statistical physics and probability theory. FKG inequality guarantees  $\text{Cov}_{Z \sim \mathcal{N}(0,1)}(f(Z), g(Z)) \geq 0$  provided that  $f, g$  are non-decreasing. Thus, a neural network built from one-dimensional linear maps and ReLU always yields nonpositive correlation with antithetic noises.

To generalize the result to higher dimension, we define a function  $f : \mathbb{R}^m \rightarrow \mathbb{R}$  to be *partially monotone* if for each coordinate  $j$ , holding all other inputs fixed, the map  $t \mapsto f(x_1, \dots, x_{j-1}, t, x_{j+1}, \dots, x_m)$  is either non-decreasing or non-increasing. Mixed monotonicity is allowed. For example,  $f(x, y) = x - y$  is non-decreasing in  $x$  and non-increasing in  $y$ , yet still qualifies as partially monotone. We have the following result:

**Proposition 1.** *For a diffusion model  $DM : \mathbb{R}^d \rightarrow \mathbb{R}^m$  and a summary statistics  $S : \mathbb{R}^m \rightarrow \mathbb{R}$ , if the joint map is partially monotone, then  $\text{Corr}(S \circ DM(Z), S \circ DM(-Z)) \leq 0$ .*

Our proof is based on an adaptation of the FKG inequality and is provided in Appendix A.2.

Proposition 1 relies on checking partial-monotonicity. If  $S$  is partially monotone (including any linear statistic), then the conditions of Proposition 1 are satisfied by, e.g., Neural Additive Models [1] and Deep Lattice Networks [60]. Unfortunately, partial-monotonicity is in general hard to verify.

While popular diffusion architectures like DiT and U-Net lack partial monotonicity, we include Proposition 1 as an expository attempt to highlight the FKG connection behind negative correlation.

## 4 Uncertainty quantification

To assess a diffusion model, one typically draws multiple initial noises, computes the desired statistic for each output, and aggregates the results into point estimates and confidence intervals, which also enables uncertainty estimation from multiple samples beyond a single run. Common statistics of interest include (i) mean pixel intensity for detecting signal leakage [22, 9] and out-of-distribution detection [20], (ii) CLIP similarity

for measuring semantic alignment in text-to-image models [3, 32], and (iii) reconstruction error across posterior samples for assessing performance and uncertainty [27, 57].

Our goal is to leverage negative correlation to design an estimator with higher accuracy at fixed cost.

**Standard Monte Carlo:** Formally, consider a diffusion model DM that maps noise to data, and a statistic  $S$ . The quantity of interest is  $\mathbb{E}_{z \sim \mathbb{N}(0, I)}[S(\text{DM}(z))]$ . To approximate this expectation, the simplest approach is to draw  $N$  independent noise samples  $z_1, \dots, z_N \sim \mathbb{N}(0, I)$ , calculate  $S_i = S(\text{DM}(z_i))$  for each  $i$  and form the standard Monte Carlo (MC) estimator  $\hat{\mu}_N^{\text{MC}} := \sum_{i=1}^N S_i/N$  by taking their average. A  $(1 - \alpha)$  confidence interval, denoted as  $\text{CI}_N^{\text{MC}}(1 - \alpha)$  is then

$$\hat{\mu}_N^{\text{MC}} \pm z_{1-\alpha/2} \sqrt{\frac{(\hat{\sigma}_N^{\text{MC}})^2}{N}},$$

where  $\hat{\sigma}_N^2$  is the sample variance of  $S_1, S_2, \dots, S_N$  and  $z_{1-\alpha/2}$  is the  $(1 - \alpha/2)$ -quantile of the standard normal. A formal guarantee of the above construction is given below:

**Proposition 2.** Denote  $\mathbb{E}_{z \sim \mathbb{N}(0, I)}[S(\text{DM}(z))]$  by  $\mu$  and  $\text{Var}_{z \sim \mathbb{N}(0, I)}[S(\text{DM}(z))]$  by  $\sigma^2$ . Assuming  $\sigma^2 < \infty$ , then we have:

- $\hat{\mu}_N^{\text{MC}} \rightarrow \mu$  and  $(\hat{\sigma}_N^{\text{MC}})^2 \rightarrow \sigma^2$  almost surely, and  $\mathbb{P}(\mu \in \text{CI}_N^{\text{MC}}(1 - \alpha)) \rightarrow 1 - \alpha$ , both as  $N \rightarrow \infty$ .
- $\mathbb{E}[(\hat{\mu}_N^{\text{MC}} - \mu)^2] = \text{Var}[\hat{\mu}_N^{\text{MC}}] = \sigma^2/N$ .

In words, the above proposition shows: (i) *Correctness*: The standard Monte Carlo estimator  $\hat{\mu}_N^{\text{MC}}$  converges to the true value, and the coverage probability of  $\text{CI}_N^{\text{MC}}(1 - \alpha)$  converges to the nominal level  $(1 - \alpha)$ . (ii) *Reliability*: The expected squared error of  $\hat{\mu}_N^{\text{MC}}$  equals the variance of a single sample divided by sample size. The confidence interval has width approximately  $2\sigma z_{1-\alpha/2}/\sqrt{N}$ .

**Antithetic Monte Carlo:** The observed negative correlation motivates an improved estimator. Let  $N = 2K$  be even, users can generate  $K$  pairs of antithetic noise  $(z_1, -z_1), \dots, (z_K, -z_K)$ . Define  $S_i^+ = S(\text{DM}(z_i))$ ,  $S_i^- = S(\text{DM}(-z_i))$ , and let  $\bar{S}_i = 0.5(S_i^+ + S_i^-)$  be their average. Our Antithetic Monte Carlo (AMC) estimator is  $\hat{\mu}_N^{\text{AMC}} := \sum_{i=1}^K \bar{S}_i/K$ , and confidence interval  $\text{CI}_N^{\text{AMC}}(1 - \alpha)$  is

$$\hat{\mu}_N^{\text{AMC}} \pm z_{1-\alpha/2} \sqrt{\frac{2(\hat{\sigma}_N^{\text{AMC}})^2}{N}},$$

where  $(\hat{\sigma}_N^{\text{AMC}})^2$  is the sample variance of  $\bar{S}_1, \dots, \bar{S}_K$ .

The intuition is simple: if the pair  $(S_i^+, S_i^-)$  remains negatively correlated, then averaging antithetic pairs can reduce variance by partially canceling out opposing errors—since

negative correlation suggests that when one estimate exceeds the true value, the other is likely to fall below it.

The AMC estimator is unbiased, and  $\text{CI}_N^{\text{AMC}}(1 - \alpha)$  achieves correct coverage as the sample size increases. Let  $\rho := \text{Corr}(S_i^+, S_i^-)$ . We can prove that AMC’s standard error and its confidence-interval width are each equal to the Monte Carlo counterparts multiplied by the factor  $\sqrt{1 + \rho}$ . Thus, when  $\rho < 0$ , AMC produces **provably lower variance and tighter confidence intervals** than MC, with greater gains as  $\rho$  becomes more negative. See Appendix A.3 for a formal statement and proof.

Since both methods have the same computational cost, the variance reduction from negative correlation and the antithetic design yields a direct and cost-free improvement.

### Quasi-Monte Carlo:

The idea of using negatively correlated samples has been widely adopted in Monte Carlo methods [8] and statistical risk estimation [25] for improved performance. Generalizing beyond paired correlation, one could generate  $N$  negatively correlated Gaussian noises  $z_1, \dots, z_N$  with  $\text{Corr}(z_j, z_k) = -1/(N - 1)$  for  $j \neq k$ . When  $N = 2$ , this recovers our antithetic sampling.

This principle of variance reduction can be further extended to QMC methods. As an alternative to Monte Carlo, QMC constructs a deterministic set of  $N$  samples that have negative correlation and provide a more balanced coverage of the sample space. QMC samples can also be randomized, resulting in RQMC methods. RQMC maintains the marginal distribution of each sample while preserving the low-discrepancy properties of QMC. Importantly, repeated randomizations allow for empirical error estimation and confidence intervals [29].

With negative correlation ( $\rho < 0$ ), AMC improves the variance by a *constant factor* of  $1 + \rho$ . In contrast, under regularity conditions [33], QMC and RQMC can improve the error *convergence rate* from  $O(N^{-1/2})$  to  $O(N^{-1+\epsilon})$  for any  $\epsilon > 0$ , albeit  $\epsilon$  may absorb a dimension-dependent factor  $(\log N)^d$ . For sufficiently smooth functions, RQMC can even achieve rates as fast as  $O(N^{-3/2+\epsilon})$  [34, 35]. Moreover, the space-filling nature of QMC may also lead to more diverse sample generation.

Although the dimension of the Gaussian noise is higher than the typical regime where QMC is expected to be most effective, RQMC still further shrinks our confidence intervals by several-fold compared with standard MC. This hints that the image generator’s effective dimension is much lower than its ambient one, allowing QMC methods to stay useful. Similar gains arise when QMC methods deliberately exploit low-dimensional structure in practical problems [56, 59, 24]. Developing ways to identify and leverage this structure more systematically is an appealing avenue for future work.

## 5 Experiments

We apply the antithetic-noise approach to the two tasks introduced in Section 1: image diversity and uncertainty quantification. Throughout this section, we evaluate our method across three settings: (1) unconditional diffusion models on standard datasets, (2) text-to-image generation using Stable Diffusion, and (3) measurement-guided generation via Diffusion Posterior Sampling (DPS).

We use pretrained models from Hugging Face’s Diffusers library [53]: google/ddpm-church-256, google/ddpm-cifar10-32, and google/ddpm-celebahq-256 for unconditional diffusion; Stable Diffusion v1.5 for text-to-image; and the original repository from [7] for guided generation. Experiments were run on eight NVIDIA L40 GPUs. The most intensive setup—Stable Diffusion—takes about five minutes to generate 100 images for a single prompt.

### 5.1 Improving diversity

Many diffusion tools generate a few images from one prompt to let users select a preferred one. For example, DALL·E 3 via ChatGPT interface outputs two images, Kera.ai outputs three, and Midjourney outputs four. However, these images often look similar and are thus less useful [30, 41].

We show that antithetic noise yields more diverse images compared with independent noise, with no loss in image quality or extra computational cost. We expect our method can be easily integrated into existing diversity optimization techniques to further improve their performance. We quantify diversity by computing pairwise SSIM to measure structural similarity (lower = more diverse) and LPIPS [62] (higher = more diverse) to capture perceptual distance in deep feature space.

We begin with unconditional image generation using pre-trained diffusion models on standard datasets. We prepare 1,600 PN noise pairs (antithetic) and 1,600 RR noise pairs (independent) as inputs and generate images with a 50-step DDIM sampler.

The diversity metrics are computed for each pair. As shown in Table 2, antithetic noise pairs consistently lead to higher diversity, as indicated by lower SSIM and higher LPIPS scores. Importantly, image quality remains stable for both noise types. For example, on CIFAR10, the mean MUSIQ scores are 16.82 for PN and 16.78 for RR. This suggests that the increased diversity introduced by antithetic noise does not come at the cost of visual quality.

We next evaluate our method using Stable Diffusion with 20-step DDIM. We evaluate the model on a total of 200 prompts selected from the Pick-a-Pic [17] and DrawBench benchmarks [42]. For each prompt, we generate 100 image pairs using antithetic and

independent initial noises respectively. As in the unconditional setting, antithetic noise consistently results in greater diversity, shown in Table 2, while still preserving semantic alignment with the prompt indicated by CLIP scores of 30.07 (PN) and 30.06 (RR). Notably, the improvement holds for *nearly all prompts*; for instance, SSIM improved in 199 out of 200 prompts, and we suspect the only remaining case is due to statistical fluctuation.

Table 2: *Average percentage improvement* of PN pairs over RR pairs on SSIM and LPIPS.

Metric	Unconditional Diffusion			Stable Diffusion	
	CIFAR-10	LSUN-Church	CelebA-HQ	DrawBench	Pick-a-Pic
SSIM (%)	86.1422	34.0056	32.8561	21.511	19.0020
LPIPS (%)	8.2881	4.2029	18.1126	4.8170	5.3613

## 5.2 Uncertainty quantification

We compute various statistics using MC, AMC, and QMC estimators discussed in Section 4.

We define the *relative efficiency* of method A with respect to the standard MC baseline as the squared ratio of their confidence interval (CI) lengths,  $(CI_{MC}/CI_A)^2$ . Since standard MC produces CIs of length  $O(N^{-1/2})$ , the relative efficiency quantifies how many more MC samples are required to match the A’s CI length. For each method, we report both the 95% CI width and its relative efficiency.

### 5.2.1 Estimating pixel-wise statistics

The custom statistics include: pixel value mean (the average intensity across all pixels), perceived brightness (computed via a luminance-weighted combination of RGB channels), contrast (the difference in brightness between the top and bottom halves of the image), and image centroid (the vertical coordinate of the intensity mass center), detailed definitions are in Appendix B.3.

To ensure equal cost, we fix a budget of 3,200 samples for unconditional diffusion model and 200 samples/prompt for Stable Diffusion (across 200 prompts). Therefore, for unconditional diffusion, the MC estimator uses 3,200 independent samples; the AMC estimator uses 1,600 pairs from antithetic noises ( $1,600 \times 2 = 3,200$ ); and QMC uses a Sobol’ point set of size 64 and applies 50 independent randomization ( $50 \times 64 = 3,200$ ). For Stable Diffusion, MC uses 200 independent samples; AMC uses 100 pairs; and QMC uses 8 Sobol’ points and 25 independent randomization. For MC and AMC, CIs are constructed as discussed in Section 4. For QMC, since the number of replicates is relatively

small, we use the student- $t$  CI to ensure reliable coverage [29]. The Sobol’ sequence uses direction numbers from [13], where the maximum number of dimensions is 21,201, limiting our QMC implementation to CIFAR-10 and Stable Diffusion. Details on RQMC CIs are in Appendix B.3.

Across all statistics, both AMC and QMC achieve much shorter CIs than MC, with relative efficiencies ranging from 3.1 to 136. This strongly suggests our proposed method can dramatically reduce the number of samples needed for reliable uncertainty estimates. AMC and QMC estimators often yield comparable results. The performance of QMC depends on how the total budget is allocated between the size of the QMC point set and the number of random replicates, a trade-off we explore in B.3.

Table 3: CI lengths and efficiency  $(CI_{MC}/CI)^2$  (in parentheses), using MC as baseline.

Dataset		Brightness	Pixel Mean	Contrast	Centroid
Stable Diff.	MC	5.45	5.59	2.18	4.03
	QMC	1.35 (16.13)	1.42 (15.23)	1.03 (4.46)	1.88 (4.54)
	AMC	<b>1.26 (18.83)</b>	<b>1.41 (15.84)</b>	<b>0.89 (6.25)</b>	<b>1.62 (6.15)</b>
CIFAR10	MC	2.00	2.04	1.08	0.11
	QMC	0.35 (32.05)	0.39 (26.94)	<b>0.22 (23.43)</b>	<b>0.04 (7.35)</b>
	AMC	<b>0.35 (32.66)</b>	<b>0.39 (27.12)</b>	0.23 (22.05)	0.04 (6.96)
CelebA	MC	1.82	1.76	0.60	0.60
	AMC	<b>0.26 (50.16)</b>	<b>0.31 (33.15)</b>	<b>0.19 (10.18)</b>	<b>0.20 (8.27)</b>
Church	MC	1.67	1.67	1.02	0.70
	AMC	<b>0.14 (136.37)</b>	<b>0.16 (106.79)</b>	<b>0.20 (27.16)</b>	<b>0.40 (3.14)</b>

### 5.2.2 Estimating reconstruction uncertainty in Bayesian inverse problems

In Bayesian inverse problems, where the goal is to recover a clean image from a corrupted observation, we aim to reliably estimate the expected reconstruction quality and uncertainty of a posterior sampling algorithm. In this work, we focus on DPS [7]. Reconstruction error is measured using PSNR and L1 distance to true image. We use 200 human face images

from the CelebA-HQ dataset as ground truth, and consider the inpainting task (details in Appendix B.3). For each corrupted image, we generate 50 DPS reconstructions using PN and RR noise pairs and compare their estimates. They both give consistent results,

Table 4: Reconstruction uncertainty in L1 and PSNR

Metric	Group	Mean	CI Length	Eff.
L1	AMC	21.86	<b>0.83</b>	1.54
	MC	21.98	1.03	
PSNR	AMC	19.03	<b>0.26</b>	1.71
	MC	18.98	0.34	

with AMC being 54% – 71% more efficient, though with smaller gains than earlier cases. Other tasks are reported in Appendix B.3.

## 6 Potential, limitations, and future directions

We find that antithetic initial noise yields negatively correlated samples. This finding enables us to improve sample diversity and construct more accurate estimators. However, our method is not a panacea: the LPIPS diversity gains in Table 2 are consistent but moderate. Although we greatly improve pixel-wise statistic estimates, our method yields very small gains (often 1%) on neural-network-based metrics like MUSIQ and CLIP Score versus standard Monte Carlo, since the Transformers’ strong nonlinearity absorbs most of the diffusion outputs’ negative correlation.

Looking forward, future directions include systematically testing the symmetry conjecture; integrating antithetic noise with existing noise-optimization methods to enhance performance; and further leveraging the strengths of QMC to improve sampling and estimation.

## Acknowledgement

Guanyang Wang acknowledges support from the National Science Foundation through grant DMS-2210849 and an Adobe Data Science Research Award. Bowen Song and Liyue Shen acknowledge support from University of Michigan MICDE (Michigan Institute for Computational Discovery and Engineering) Catalyst Grant, and University of Michigan MIDAS (Michigan Institute for Data Science) PODS Grant.

## References

- [1] Rishabh Agarwal, Levi Melnick, Nicholas Frosst, Xuezhou Zhang, Ben Lengerich, Rich Caruana, and Geoffrey E Hinton. Neural additive models: Interpretable machine learning with neural nets. *Advances in Neural Information Processing Systems*, 34:4699–4711, 2021.
- [2] Yuanhao Ban, Ruo Chen Wang, Tianyi Zhou, Boqing Gong, Cho-Jui Hsieh, and Minhao Cheng. The crystal ball hypothesis in diffusion models: Anticipating object positions from initial noise. In *The Thirteenth International Conference on Learning Representations*, 2025.
- [3] Brinnae Bent. Semantic approach to quantifying the consistency of diffusion model image generation. In *Proceedings of the IEEE/CVF Conference on Computer Vision and Pattern Recognition*, pages 8218–8222, 2024.
- [4] Alexander Buchholz, Florian Wenzel, and Stephan Mandt. Quasi-Monte Carlo variational inference. In *International Conference on Machine Learning*, pages 668–677. PMLR, 2018.
- [5] Changgu Chen, Libing Yang, Xiaoyan Yang, Lianggangxu Chen, Gaoqi He, Changbo Wang, and Yang Li. FIND: Fine-tuning initial noise distribution with policy optimization for diffusion models. In *Proceedings of the 32nd ACM International Conference on Multimedia*, pages 6735–6744, 2024.
- [6] Siyi Chen, Huijie Zhang, Minzhe Guo, Yifu Lu, Peng Wang, and Qing Qu. Exploring low-dimensional subspace in diffusion models for controllable image editing. In *The Thirty-eighth Annual Conference on Neural Information Processing Systems*, 2024.
- [7] Hyungjin Chung, Jeongsol Kim, Michael Thompson Mccann, Marc Louis Klasky, and Jong Chul Ye. Diffusion posterior sampling for general noisy inverse problems. In *The Eleventh International Conference on Learning Representations*, 2023.
- [8] Radu V Craiu and Xiao-Li Meng. Multiprocess parallel antithetic coupling for backward and forward Markov chain Monte Carlo. *Annals of Statistics*, pages 661–697, 2005.
- [9] Martin Nicolas Everaert, Athanasios Fitsios, Marco Bocchio, Sami Arpa, Sabine Süssstrunk, and Radhakrishna Achanta. Exploiting the signal-leak bias in diffusion models. In *Proceedings of the IEEE/CVF Winter Conference on Applications of Computer Vision*, pages 4025–4034, 2024.

- [10] Cees M Fortuin, Pieter W Kasteleyn, and Jean Ginibre. Correlation inequalities on some partially ordered sets. *Communications in Mathematical Physics*, 22:89–103, 1971.
- [11] Xiefan Guo, Jinlin Liu, Miaomiao Cui, Jiankai Li, Hongyu Yang, and Di Huang. Initno: Boosting text-to-image diffusion models via initial noise optimization. In *Proceedings of the IEEE/CVF Conference on Computer Vision and Pattern Recognition*, pages 9380–9389, 2024.
- [12] Jonathan Ho, Ajay Jain, and Pieter Abbeel. Denoising diffusion probabilistic models. *Advances in neural information processing systems*, 33:6840–6851, 2020.
- [13] Stephen Joe and Frances Y Kuo. Constructing Sobol sequences with better two-dimensional projections. *SIAM Journal on Scientific Computing*, 30(5):2635–2654, 2008.
- [14] Corwin Joy, Phelim P Boyle, and Ken Seng Tan. Quasi-Monte Carlo methods in numerical finance. *Management science*, 42(6):926–938, 1996.
- [15] Tero Karras, Miika Aittala, Timo Aila, and Samuli Laine. Elucidating the design space of diffusion-based generative models. *Advances in Neural Information Processing Systems*, 35:26565–26577, 2022.
- [16] Alexander Keller. A quasi-Monte Carlo algorithm for the global illumination problem in the radiosity setting. In *Monte Carlo and Quasi-Monte Carlo Methods in Scientific Computing: Proceedings of a conference at the University of Nevada, Las Vegas, Nevada, USA, June 23–25, 1994*, pages 239–251. Springer, 1995.
- [17] Yuval Kirstain, Adam Polyak, Uriel Singer, Shahbuland Matiana, Joe Penna, and Omer Levy. Pick-a-pic: An open dataset of user preferences for text-to-image generation. In *Thirty-seventh Conference on Neural Information Processing Systems*, 2023.
- [18] Zhifeng Kong, Wei Ping, Jiaji Huang, Kexin Zhao, and Bryan Catanzaro. Diffwave: A versatile diffusion model for audio synthesis. In *International Conference on Learning Representations*, 2021.
- [19] Alex Krizhevsky, Geoffrey Hinton, et al. Learning multiple layers of features from tiny images. 2009.
- [20] Georges Le Bellier and Nicolas Audebert. Detecting out-of-distribution earth observation images with diffusion models. In *Proceedings of the IEEE/CVF Conference on Computer Vision and Pattern Recognition*, pages 481–491, 2024.

- [21] Xiang Li, Yixiang Dai, and Qing Qu. Understanding generalizability of diffusion models requires rethinking the hidden gaussian structure. *Advances in neural information processing systems*, 37:57499–57538, 2024.
- [22] Shanchuan Lin, Bingchen Liu, Jiashi Li, and Xiao Yang. Common diffusion noise schedules and sample steps are flawed. In *Proceedings of the IEEE/CVF winter conference on applications of computer vision*, pages 5404–5411, 2024.
- [23] Sifan Liu and Art B Owen. Quasi-Monte Carlo quasi-Newton in variational Bayes. *Journal of Machine Learning Research*, 22(243):1–23, 2021.
- [24] Sifan Liu and Art B Owen. Preintegration via active subspace. *SIAM Journal on Numerical Analysis*, 61(2):495–514, 2023.
- [25] Sifan Liu, Snigdha Panigrahi, and Jake A. Soloff. Cross-validation with antithetic Gaussian randomization. *arXiv preprint arXiv:2412.14423*, 2024.
- [26] Cheng Lu, Yuhao Zhou, Fan Bao, Jianfei Chen, Chongxuan Li, and Jun Zhu. DPM-solver++: Fast solver for guided sampling of diffusion probabilistic models, 2023.
- [27] Guanxiong Luo, Moritz Blumenthal, Martin Heide, and Martin Uecker. Bayesian mri reconstruction with joint uncertainty estimation using diffusion models. *Magnetic Resonance in Medicine*, 90(1):295–311, 2023.
- [28] Pierre L’Ecuyer. Quasi-Monte Carlo methods with applications in finance. *Finance and Stochastics*, 13:307–349, 2009.
- [29] Pierre L’Ecuyer, Marvin K. Nakayama, Art B. Owen, and Bruno Tuffin. Confidence intervals for randomized quasi-Monte Carlo estimators. In *2023 Winter Simulation Conference*, pages 445–446, 2023.
- [30] David Marwood, Shumeet Baluja, and Yair Alon. Diversity and diffusion: Observations on synthetic image distributions with stable diffusion. *arXiv preprint arXiv:2311.00056*, 2023.
- [31] Chenlin Meng, Yutong He, Yang Song, Jiaming Song, Jiajun Wu, Jun-Yan Zhu, and Stefano Ermon. SDEdit: Guided image synthesis and editing with stochastic differential equations. In *International Conference on Learning Representations*, 2022.
- [32] Tuna Han Salih Meral, Enis Simsar, Federico Tombari, and Pinar Yanardag. Conform: Contrast is all you need for high-fidelity text-to-image diffusion models. In *Proceedings of the IEEE/CVF Conference on Computer Vision and Pattern Recognition*, pages 9005–9014, 2024.

- [33] H. Niederreiter. *Random Number Generation and Quasi-Monte Carlo Methods*. SIAM, Philadelphia, PA, 1992.
- [34] A. B. Owen. Monte Carlo variance of scrambled net quadrature. *SIAM Journal of Numerical Analysis*, 34(5):1884–1910, 1997.
- [35] A. B. Owen. Scrambled net variance for integrals of smooth functions. *Annals of Statistics*, 25(4):1541–1562, 1997.
- [36] Art B. Owen. *Monte Carlo Theory, Methods and Examples*. <https://artowen.su.domains/mc/>, 2013.
- [37] William Peebles and Saining Xie. Scalable diffusion models with transformers. In *Proceedings of the IEEE/CVF international conference on computer vision*, pages 4195–4205, 2023.
- [38] Dustin Podell, Zion English, Kyle Lacey, Andreas Blattmann, Tim Dockhorn, Jonas Müller, Joe Penna, and Robin Rombach. SDXL: Improving latent diffusion models for high-resolution image synthesis. In *The Twelfth International Conference on Learning Representations*, 2024.
- [39] Zipeng Qi, Lichen Bai, Haoyi Xiong, and Zeke Xie. Not all noises are created equally: Diffusion noise selection and optimization. *arXiv preprint arXiv:2407.14041*, 2024.
- [40] Robin Rombach, Andreas Blattmann, Dominik Lorenz, Patrick Esser, and Björn Ommer. High-resolution image synthesis with latent diffusion models. In *Proceedings of the IEEE/CVF conference on computer vision and pattern recognition*, pages 10684–10695, 2022.
- [41] Seyedmorteza Sadat, Jakob Buhmann, Derek Bradley, Otmar Hilliges, and Roman M. Weber. CADs: Unleashing the diversity of diffusion models through condition-annealed sampling. In *The Twelfth International Conference on Learning Representations*, 2024.
- [42] Chitwan Saharia, William Chan, Saurabh Saxena, Lala Li, Jay Whang, Emily L Denton, Kamyar Ghasemipour, Raphael Gontijo Lopes, Burcu Karagol Ayan, Tim Salimans, et al. Photorealistic text-to-image diffusion models with deep language understanding. *Advances in Neural Information Processing Systems*, 35:36479–36494, 2022.
- [43] Tim Salimans and Jonathan Ho. Progressive distillation for fast sampling of diffusion models. In *International Conference on Learning Representations*, 2022.

- [44] Axel Sauer, Dominik Lorenz, Andreas Blattmann, and Robin Rombach. Adversarial diffusion distillation. In *European Conference on Computer Vision*, pages 87–103. Springer, 2024.
- [45] Jascha Sohl-Dickstein, Eric Weiss, Niru Maheswaranathan, and Surya Ganguli. Deep unsupervised learning using nonequilibrium thermodynamics. In *International conference on machine learning*, pages 2256–2265. pmlr, 2015.
- [46] Bowen Song, Soo Min Kwon, Zecheng Zhang, Xinyu Hu, Qing Qu, and Liyue Shen. Solving inverse problems with latent diffusion models via hard data consistency. In *The Twelfth International Conference on Learning Representations*, 2024.
- [47] Bowen Song, Zecheng Zhang, Zhaoxu Luo, Jason Hu, Wei Yuan, Jing Jia, Zhengxu Tang, Guanyang Wang, and Liyue Shen. Ccs: Controllable and constrained sampling with diffusion models via initial noise perturbation. *arXiv preprint arXiv:2502.04670*, 2025.
- [48] Jiaming Song, Chenlin Meng, and Stefano Ermon. Denoising diffusion implicit models. In *International Conference on Learning Representations*, 2021.
- [49] Yang Song, Prafulla Dhariwal, Mark Chen, and Ilya Sutskever. Consistency models. In *International Conference on Machine Learning*, pages 32211–32252. PMLR, 2023.
- [50] Yang Song, Liyue Shen, Lei Xing, and Stefano Ermon. Solving inverse problems in medical imaging with score-based generative models. In *International Conference on Learning Representations*, 2022.
- [51] Yang Song, Jascha Sohl-Dickstein, Diederik P Kingma, Abhishek Kumar, Stefano Ermon, and Ben Poole. Score-based generative modeling through stochastic differential equations. In *International Conference on Learning Representations*, 2021.
- [52] Roman Vershynin. *High-dimensional probability: An introduction with applications in data science*, volume 47. Cambridge university press, 2018.
- [53] Patrick von Platen, Suraj Patil, Anton Lozhkov, Pedro Cuenca, Nathan Lambert, Kashif Rasul, Mishig Davaadorj, Dhruv Nair, Sayak Paul, William Berman, Yiyi Xu, Steven Liu, and Thomas Wolf. Diffusers: State-of-the-art diffusion models. <https://github.com/huggingface/diffusers>, 2022.
- [54] Carsten Waechter and Alexander Keller. Quasi-Monte Carlo light transport simulation by efficient ray tracing, May 31 2011. US Patent 7,952,583.

- [55] Binxu Wang and John Vastola. The unreasonable effectiveness of gaussian score approximation for diffusion models and its applications. *Transactions on Machine Learning Research*, 2024.
- [56] Xiaoqun Wang and Kai-Tai Fang. The effective dimension and quasi-Monte Carlo integration. *Journal of Complexity*, 19:101–124, 2003.
- [57] Di Wu, Shicai Fan, Xue Zhou, Li Yu, Yuzhong Deng, Jianxiao Zou, and Baihong Lin. Unsupervised anomaly detection via masked diffusion posterior sampling. In *Proceedings of the Thirty-Third International Joint Conference on Artificial Intelligence*, pages 2442–2450, 2024.
- [58] Weihao Xia, Yujiu Yang, Jing-Hao Xue, and Baoyuan Wu. Tedigan: Text-guided diverse face image generation and manipulation. In *IEEE Conference on Computer Vision and Pattern Recognition (CVPR)*, 2021.
- [59] Ye Xiao and Xiaoqun Wang. Enhancing quasi-Monte Carlo simulation by minimizing effective dimension for derivative pricing. *Computational Economics*, 54(1):343–366, 2019.
- [60] Seungil You, David Ding, Kevin Canini, Jan Pfeifer, and Maya Gupta. Deep lattice networks and partial monotonic functions. *Advances in neural information processing systems*, 30, 2017.
- [61] Fisher Yu, Ari Seff, Yinda Zhang, Shuran Song, Thomas Funkhouser, and Jianxiong Xiao. Lsun: Construction of a large-scale image dataset using deep learning with humans in the loop. *arXiv preprint arXiv:1506.03365*, 2015.
- [62] Richard Zhang, Phillip Isola, Alexei A Efros, Eli Shechtman, and Oliver Wang. The unreasonable effectiveness of deep features as a perceptual metric. In *Proceedings of the IEEE conference on computer vision and pattern recognition*, pages 586–595, 2018.
- [63] Zikai Zhou, Shitong Shao, Lichen Bai, Zhiqiang Xu, Bo Han, and Zeke Xie. Golden noise for diffusion models: A learning framework. *arXiv preprint arXiv:2411.09502*, 2024.

## A Proofs

### A.1 Proofs in Section 3.2

*Proof of Lemma 1.* It suffices to show  $\text{Var}(f(Z) + f(-Z)) = 0$ . By definition:

$$\text{Corr}(f(-Z), f(Z)) = \frac{\text{Cov}(f(-Z), f(Z))}{\sqrt{\text{Var}(f(Z)) \text{Var}(f(-Z))}} = -1.$$

Therefore

$$\begin{aligned} \text{Var}(f(Z) + f(-Z)) &= \text{Var}(f(Z)) + \text{Var}(f(-Z)) + 2 \text{Cov}(f(Z), f(-Z)) \\ &= \text{Var}(f(Z)) + \text{Var}(f(-Z)) - 2\sqrt{\text{Var}(f(Z)) \text{Var}(f(-Z))} \\ &= \left( \sqrt{\text{Var}(f(Z))} - \sqrt{\text{Var}(f(-Z))} \right)^2. \end{aligned}$$

On the other hand, since  $-Z \sim \mathbb{N}(0, I)$  given  $Z \sim \mathbb{N}(0, 1)$ , we have  $\text{Var}(f(Z)) = \text{Var}(f(-Z))$  and then  $\text{Var}(f(Z) + f(-Z)) = 0$ , as claimed.  $\square$

### A.2 Proofs in Section 3.3

We first formally state and prove the claim for the univariate case in Section 3.3.

**Proposition 3** (Univariate case). *Let  $z \sim \mathbb{N}(0, 1)$  and let  $F : \mathbb{R} \rightarrow \mathbb{R}$  be the output of any one-dimensional feed-forward network obtained by alternating scalar linear maps and ReLU activations:*

$$h_0(z) = z, \quad h_\ell(z) = \text{ReLU}(w_\ell h_{\ell-1}(z) + b_\ell), \quad \ell = 1, \dots, L, \quad F(z) = h_L(z).$$

*For all choices of depths  $L$  and coefficients  $\{w_\ell, b_\ell\}_{\ell=1}^L$ ,*

$$\text{Corr}(F(z), F(-z)) \leq 0.$$

*Proof.* An important observation is that monotonicity is preserved under composition: combining one monotonic function with another produces a function that remains monotonic.

Each scalar linear map  $x \mapsto w_\ell x + b_\ell$  is monotone: it is non-decreasing if  $w_\ell \geq 0$  and non-increasing if  $w_\ell < 0$ . The ReLU map  $x \mapsto \text{ReLU}(x) = \max\{0, x\}$  is non-decreasing. Hence the final function  $F$  is monotone. Without loss of generality, we assume  $F$  is non-decreasing.

FKG inequality guarantees  $\text{Cov}_{Z \sim \mathbb{N}(0,1)}(f(Z), g(Z)) \geq 0$  provided that  $f, g$  are non-

decreasing. Therefore,  $\text{Cov}_{Z \sim \mathbb{N}(0,1)}(F(Z), F(-Z)) = -\text{Cov}_{Z \sim \mathbb{N}(0,1)}(F(Z), -F(-Z)) \leq 0$ . Since

$$\text{Corr}(F(z), F(-z)) = \frac{\text{Cov}_{Z \sim \mathbb{N}(0,1)}(F(Z), F(-Z))}{\sqrt{\text{Var}(F(z)) \text{Var}(F(-z))}},$$

we have  $\text{Corr}(F(z), F(-z)) \leq 0$ . □

Now we prove the general case:

*Proof of Proposition 1.* Let  $G := S \circ \text{DM}$ . For each coordinate  $j \in [d]$  fix a sign

$$s_j = \begin{cases} +1, & \text{if } G \text{ is non-decreasing in } x_j, \\ -1, & \text{if } G \text{ is non-increasing in } x_j. \end{cases}$$

Write  $s = (s_1, \dots, s_d) \in \{\pm 1\}^d$  and define, for any  $z \in \mathbb{R}^d$ ,

$$\tilde{G}(z) = \tilde{G}(z_1, \dots, z_d) := G(s_1 z_1, \dots, s_d z_d).$$

Similarly, define

$$\tilde{H}(z) := \tilde{G}(-z) = G(-s_1 z_1, \dots, -s_d z_d).$$

By construction,  $\tilde{G}$  is coordinate-wise non-decreasing and  $\tilde{H}$  is coordinate-wise non-increasing.

Because each coordinate of  $Z \sim \mathbb{N}(0, I_d)$  is symmetric, the random vectors  $(s_1 Z_1, \dots, s_d Z_d)$  and  $(Z_1, \dots, Z_d)$  have the same distribution. Hence

$$\text{Cov}(G(Z), G(-Z)) = \text{Cov}(\tilde{G}(Z), \tilde{H}(Z)).$$

The multivariate FKG inequality [10] for product Gaussian measures states that, when  $U$  and  $V$  are coordinate-wise non-decreasing,  $\text{Cov}(U(Z), V(Z)) \geq 0$ . Apply it to the pair  $(\tilde{G}, -\tilde{H})$ : both components are non-decreasing, so

$$\text{Cov}(\tilde{G}(Z), -\tilde{H}(Z)) \geq 0 \implies \text{Cov}(\tilde{G}(Z), \tilde{H}(Z)) \leq 0 \Leftrightarrow \text{Cov}(G(Z), G(-Z)) \leq 0.$$

Therefore  $\text{Corr}(G(Z), G(-Z)) \leq 0$ , as claimed. □

## A.3 Proofs in Section 4

### A.3.1 Monte Carlo estimator:

*Proof of Proposition 2.* Let  $S_i := S(\text{DM}(z_i))$  for  $i = 1, \dots, N$ . Because the noises  $z_i$  are drawn independently from  $\mathbb{N}(0, I)$ , the random variables  $S_1, S_2, \dots$  are independent and

identically distributed with mean  $\mu$  and variance  $\sigma^2 < \infty$ .

**Consistency.** By the *strong law of large numbers*,

$$\hat{\mu}_N^{\text{MC}} = \frac{1}{N} \sum_{i=1}^N S_i \xrightarrow{\text{a.s.}} \mu.$$

The sample variance estimator

$$(\hat{\sigma}_N^{\text{MC}})^2 = \frac{1}{N-1} \sum_{i=1}^N (S_i - \hat{\mu}_N^{\text{MC}})^2 = \frac{1}{N-1} \sum_{i=1}^N S_i^2 - \frac{N}{N-1} (\hat{\mu}_N^{\text{MC}})^2.$$

The first term converges to  $\mathbb{E}[S_1^2]$  almost surely by the law of large numbers, the second term converges to  $\mu^2$  almost surely as shown above. Therefore  $(\hat{\sigma}_N^{\text{MC}})^2 \xrightarrow{\text{a.s.}} \sigma^2$ .

**Asymptotic normality and coverage.** The classical *central limit theorem* states that

$$\sqrt{N} \frac{\hat{\mu}_N^{\text{MC}} - \mu}{\sigma} \xrightarrow{d} \mathbb{N}(0, 1).$$

Replacing the unknown  $\sigma$  by the consistent estimator  $\hat{\sigma}_N^{\text{MC}}$  and applying *Slutsky's theorem* yields

$$\sqrt{N} \frac{\hat{\mu}_N^{\text{MC}} - \mu}{\hat{\sigma}_N^{\text{MC}}} \xrightarrow{d} \mathbb{N}(0, 1).$$

Hence

$$\mathbb{P}(\mu \in \text{CI}_N^{\text{MC}}(1 - \alpha)) = \mathbb{P}\left(\left|\sqrt{N}(\hat{\mu}_N^{\text{MC}} - \mu)/\hat{\sigma}_N^{\text{MC}}\right| \leq z_{1-\alpha/2}\right) \rightarrow 1 - \alpha.$$

**Mean-squared error.** Because  $\hat{\mu}_N^{\text{MC}}$  is the average of  $N$  i.i.d. variables,

$$\text{Var}[\hat{\mu}_N^{\text{MC}}] = \frac{\sigma^2}{N}.$$

Moreover, since  $\hat{\mu}_N^{\text{MC}}$  is unbiased ( $\mathbb{E}[\hat{\mu}_N^{\text{MC}}] = \mu$ ), its mean-squared error

$$\mathbb{E}[(\hat{\mu}_N^{\text{MC}} - \mu)^2] = \mathbb{E}[(\hat{\mu}_N^{\text{MC}} - \mathbb{E}[\hat{\mu}_N^{\text{MC}}])^2] = \frac{\sigma^2}{N}.$$

This completes the proof. □

### A.3.2 Antithetic Monte Carlo Estimator:

**Proposition 4.** Denote  $\mathbb{E}[S(DM(z))]$  by  $\mu$ ,  $\text{Var}[S(DM(z))]$  by  $\sigma^2$ , and  $\text{Cov}(S_1^+, S_1^-)$  by  $\rho$ . Assuming  $\sigma^2 < \infty$ , then we have:

- $\hat{\mu}_N^{AMC} \rightarrow \mu$  and  $(\hat{\sigma}_N^{AMC})^2 \rightarrow (1 + \rho)\sigma^2/2$  almost surely as  $N \rightarrow \infty$ ,
- $\mathbb{E}[(\mu_N^{AMC} - \mu)^2] = \text{Var}[\mu_N^{AMC}] = \sigma^2(1 + \rho)/N$ .
- $\mathbb{P}(\mu \in CI_N^{AMC}(1 - \alpha)) \rightarrow 1 - \alpha$  as  $N \rightarrow \infty$ .

*Proof.* Let  $N = 2K$  and generate independent antithetic noise pairs  $(z_i, -z_i)$  for  $i = 1, \dots, K$ . Recall

$$S_i^+ = S(\text{DM}(z_i)), \quad S_i^- = S(\text{DM}(-z_i)), \quad \bar{S}_i = \frac{1}{2}(S_i^+ + S_i^-), \quad i = 1, \dots, K.$$

Because the pairs are independent and identically distributed (i.i.d.), the random variables  $\bar{S}_1, \dots, \bar{S}_K$  are i.i.d. with

$$\mathbb{E}[\bar{S}_1] = \mu$$

and

$$\text{Var}[\bar{S}_1] = \text{Var}\left[\frac{1}{2}(S_1^+ + S_1^-)\right] \tag{3}$$

$$= \left(\frac{1}{2}\right)^2 \text{Var}[S_i^+ + S_i^-] \tag{4}$$

$$= \frac{1}{4} \left( \text{Var}[S_i^+] + \text{Var}[S_i^-] + 2 \text{Cov}(S_i^+, S_i^-) \right) \tag{5}$$

$$= \frac{1}{4} \left( \sigma^2 + \sigma^2 + 2\rho\sigma^2 \right) \tag{6}$$

$$= \frac{1 + \rho}{2} \sigma^2. \tag{7}$$

where we have written  $\text{Cov}(S_i^+, S_i^-) = \rho\sigma^2$  as in the statement. Set  $\hat{\mu}_N^{AMC} = K^{-1} \sum_{i=1}^K \bar{S}_i$  and let  $(\hat{\sigma}_N^{AMC})^2$  be the sample variance of  $\bar{S}_1, \dots, \bar{S}_K$ . All three claims in Proposition 4 follow from Proposition 2. □

## B Additional Experiments

### B.1 Additional experiments on Pixel-Wise Correlations

#### B.1.1 DDPM

**Antithetic sampling setup:** Unlike DDIM, where the sampling trajectory is deterministic once the initial noise is fixed, DDPM adds a random Gaussian noise at every

timestep. The update function in DDPM is

$$x_{t-1} = \frac{1}{\sqrt{\alpha_t}} \left( x_t - \frac{1 - \alpha_t}{\sqrt{1 - \alpha_t}} \epsilon_\theta(x_t, t) \right) + \sigma_t z_t$$

and  $z_t \sim \mathcal{N}(0, 1)$  if  $t > 1$ , else  $z = 0$ . Therefore, in DDPM, antithetic sampling requires not only negating the initial noise but also negating *every noise*  $z_t$  added at each iteration.

Table 5 reports Pearson correlations between pixel values of image pairs produced using the same pre-trained models under PN and RR noise schemes using DDPM (default 1000 steps) across CIFAR10, CelebA-HQ, and LSUN-Church. For each dataset, we follow the same setup explained in Section 3. We calculate the pixelwise correction with 1600 antithetic noise pairs and 1600 independent noises.

With the same behavior in DDIM, in DDPM sampling, PN pairs also consistently exhibit lower correlation than RR pairs. The mean correlation for PN pairs is strongly negative in all datasets—CIFAR10 ( $-0.73$ ), Church ( $-0.45$ ), and in the more identity-consistent CelebA ( $-0.18$ ). In addition, the 75th percentile of PN pairs remains below zero in all datasets, with a high of  $-0.05$  (CelebA), meaning that even the upper quartile of PN correlations is still less than the average RR correlation.

Table 5: DDPM Pearson correlation coefficients for PN (pos–neg) and RR (rand–rand) pairs

Statistic	CIFAR10		CelebA		Church	
	PN	RR	PN	RR	PN	RR
<b>Mean</b>	-0.73	0.04	-0.18	0.29	-0.45	0.11
<b>Min</b>	-0.95	-0.61	-0.80	-0.50	-0.90	-0.60
<b>25th percentile</b>	-0.81	-0.12	-0.31	0.16	-0.55	-0.02
<b>75th percentile</b>	-0.66	0.20	-0.05	0.44	-0.36	0.23
<b>Max</b>	-0.21	0.80	0.44	0.78	0.07	0.80

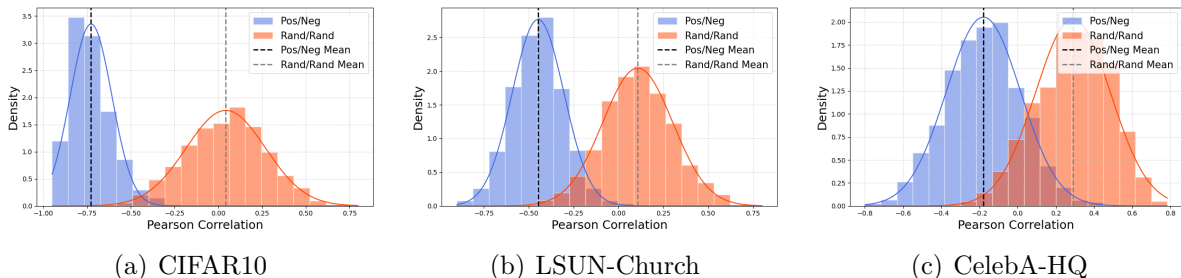


Figure 5: Pearson Correlation histograms for PN and RR pairs across three datasets using DDPM. Dashed lines indicate the mean Pearson correlation for each group.

### B.1.2 DPS

The same pattern persists in the DPS setting, too. Since DPS is guided using a reference image and there is a ground truth image available, the pixel-wise correlation is calculated using the difference between reconstructed images and the corresponding ground truth. Although the overall correlation values are shifted up—due to the deterministic conditioning and the posterior nature of sampling—PN pairs still show significantly lower correlations than RR pairs across all tasks (Inpainting, Super-resolution, Motion Deblurring).

The mean PN correlations range from 0.20 to 0.27, while RR correlations consistently lie above 0.50. Importantly, the entire PN distribution remains consistently below the RR distribution: for every task, the 75th percentile of PN correlations is less than the 25th percentile of RR correlations.

Table 6: DPS Pearson correlation coefficients for PN and RR pairs

Statistic	Inpainting		Super-resolution		Motion Deblur	
	PN	RR	PN	RR	PN	RR
<b>Mean</b>	0.27	0.57	0.20	0.53	0.25	0.55
<b>Min</b>	-0.14	0.18	-0.34	0.01	-0.32	-0.02
<b>25th percentile</b>	0.19	0.52	0.10	0.47	0.15	0.49
<b>75th percentile</b>	0.36	0.63	0.30	0.60	0.35	0.62
<b>Max</b>	0.66	0.82	0.64	0.80	0.69	0.81

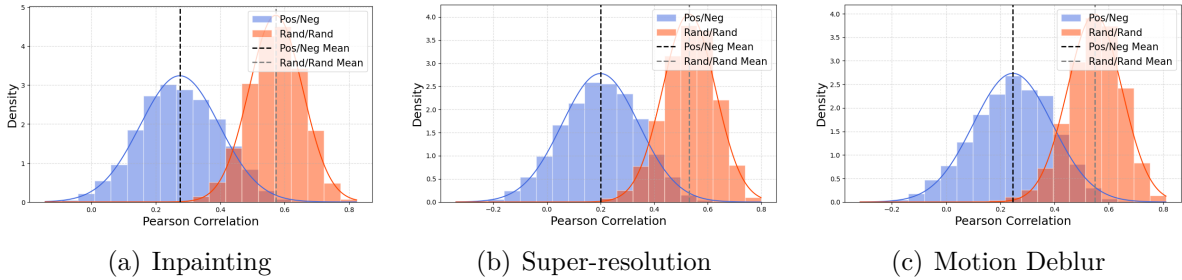


Figure 6: Pearson Correlation histograms for PN and RR pairs across three tasks in DPS. Dashed lines indicate the mean Pearson correlation for each group.

## B.2 Additional experiments on the symmetry conjecture

We run additional experiments to validate the conjecture in Section 3.2. Using a pretrained score network and a 50-step DDIM sampler, we evaluated both CIFAR-10 and Church. For each dataset, we selected five random coordinates in the  $C \times H \times W$  tensor (channel, height, width). At every chosen coordinate we examined the network output at time steps  $t = 1, \dots, 20$  (small  $t$  is close to the final image, large  $t$  is close to pure noise). For each  $t$  we drew a standard Gaussian sample  $\mathbf{x} \sim \mathbb{N}(0, I_d)$  and computed the value of  $\epsilon_\theta^{(t)}(c\mathbf{x})$  at the selected coordinate. The resulting plots appear in Figures 7–16.

To measure how much a one-dimensional function resembles an antisymmetric shape, we introduce the *affine antisymmetry score*

$$\text{AS}(f) := 1 - \frac{\int_{-1}^1 (0.5f(-x) + 0.5f(x) - \bar{f})^2}{\int_{-1}^1 (f(x) - \bar{f})^2}$$

where  $\bar{f} := \int_{-1}^1 f dx / 2$  is the average value of  $f$  on  $[-1, 1]$ .

The integral’s numerator is the squared average distance between the antithetic mean  $0.5f(-x) + 0.5f(x)$  and the overall mean  $\bar{f}$ , while the denominator is the full variance of  $f$  over the interval.

The antisymmetry score is well-defined for every non-constant function  $f$ ; it takes values in the range  $[0, 1]$  and represents the fraction of the original variance that is eliminated by antithetic averaging. The score attains  $\text{AS}(f) = 1$  exactly when the antithetic sum  $f(x) + f(-x)$  is constant, that is, when  $f$  is perfectly *affine-antisymmetric*. Conversely,  $\text{AS}(f) = 0$  if and only if  $f(-x) = f(x) + c$  for some constant  $c$ , meaning  $f$  is *affine-symmetric*.

For each dataset we have 100 (5 coordinates  $\times$  20 time steps) scalar functions; the summary statistics of their AS scores are listed in Table 7. Both datasets have very high AS scores: the means exceed 0.99 and the 10% quantiles are above 0.97, indicating that antithetic pairing eliminates nearly all variance in most cases. Even the lowest scores (about 0.77) still remove more than three-quarters of the variance.

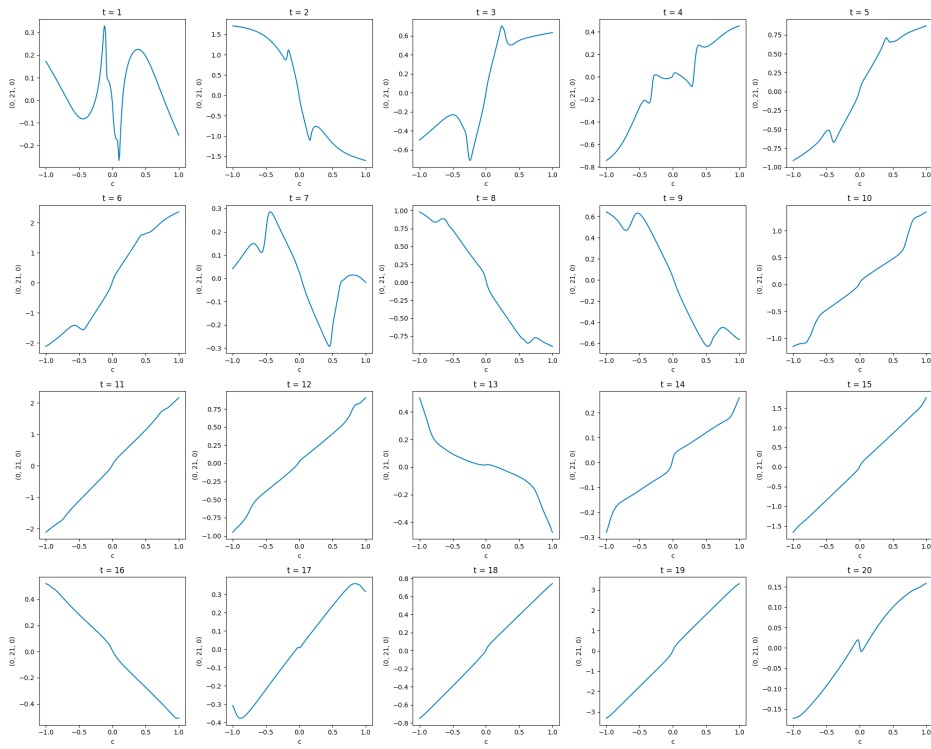


Figure 7: CIFAR10: Coordinate (0, 21, 0)

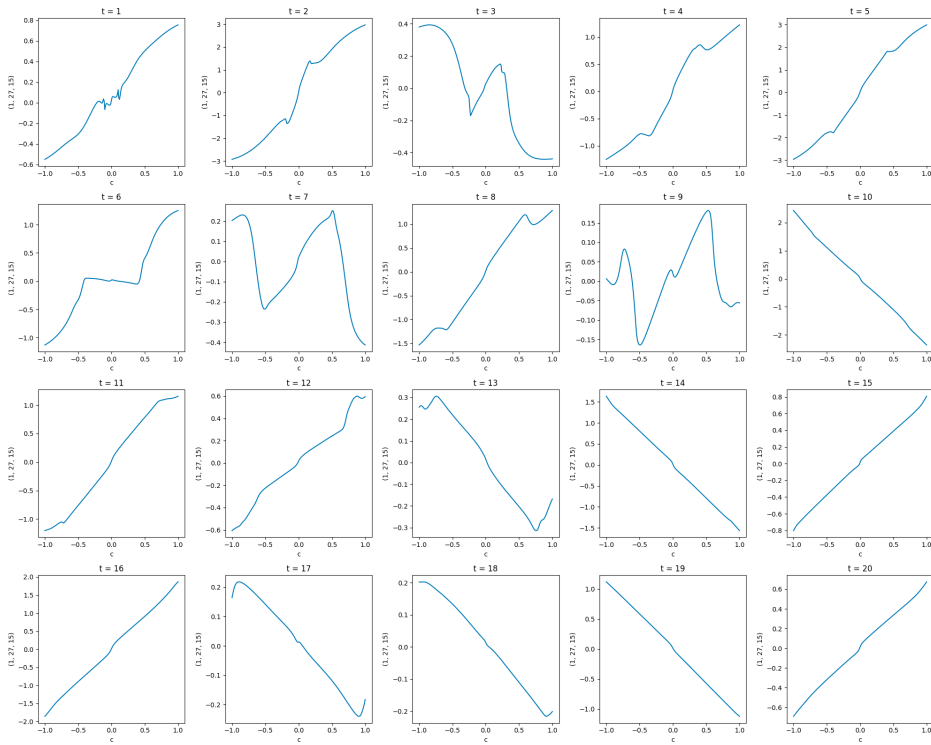


Figure 8: CIFAR10: Coordinate (1, 27, 15)

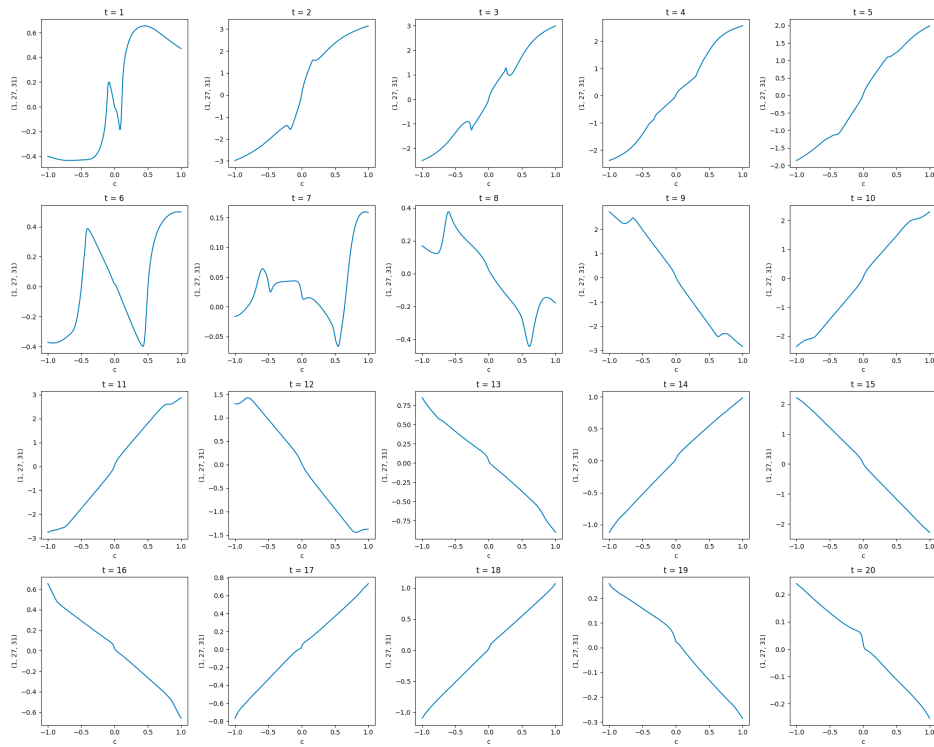


Figure 9: CIFAR10: Coordinate (1, 27, 31)

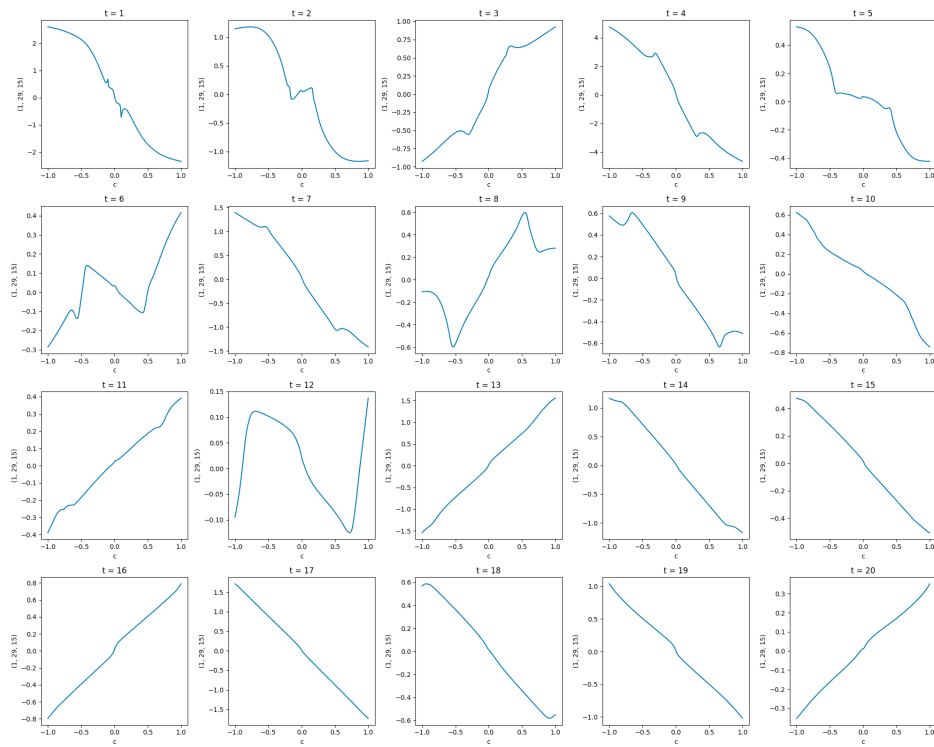


Figure 10: CIFAR10: Coordinate (1, 29, 15)

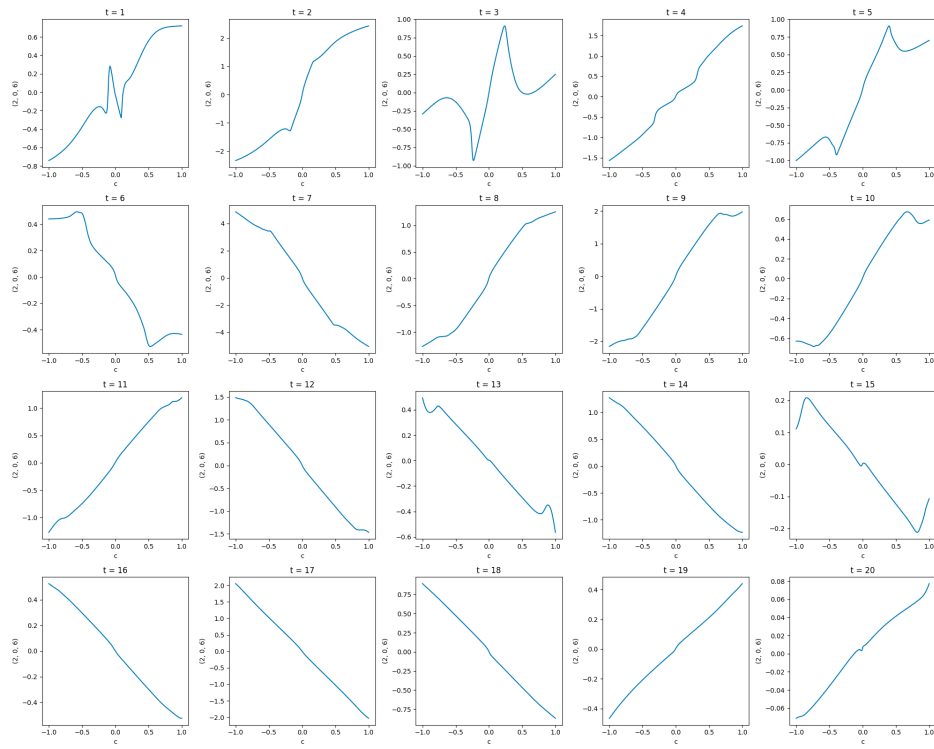


Figure 11: CIFAR10: Coordinate (2, 0, 6)

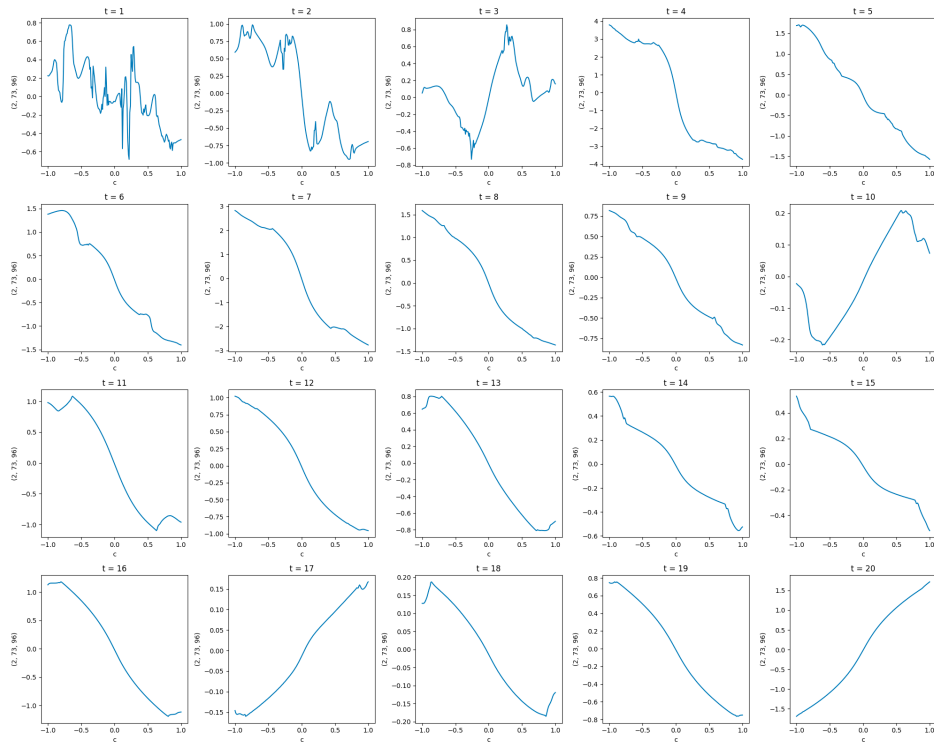


Figure 12: Church: Coordinate (2, 73, 76)

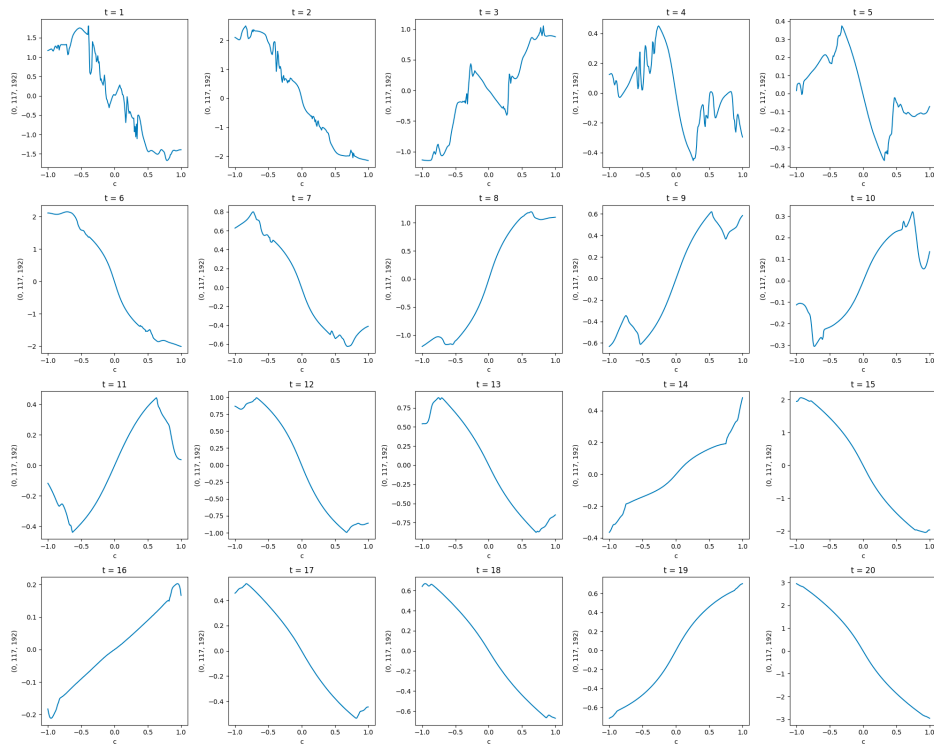


Figure 13: CIFAR10: Coordinate (0, 117, 192)

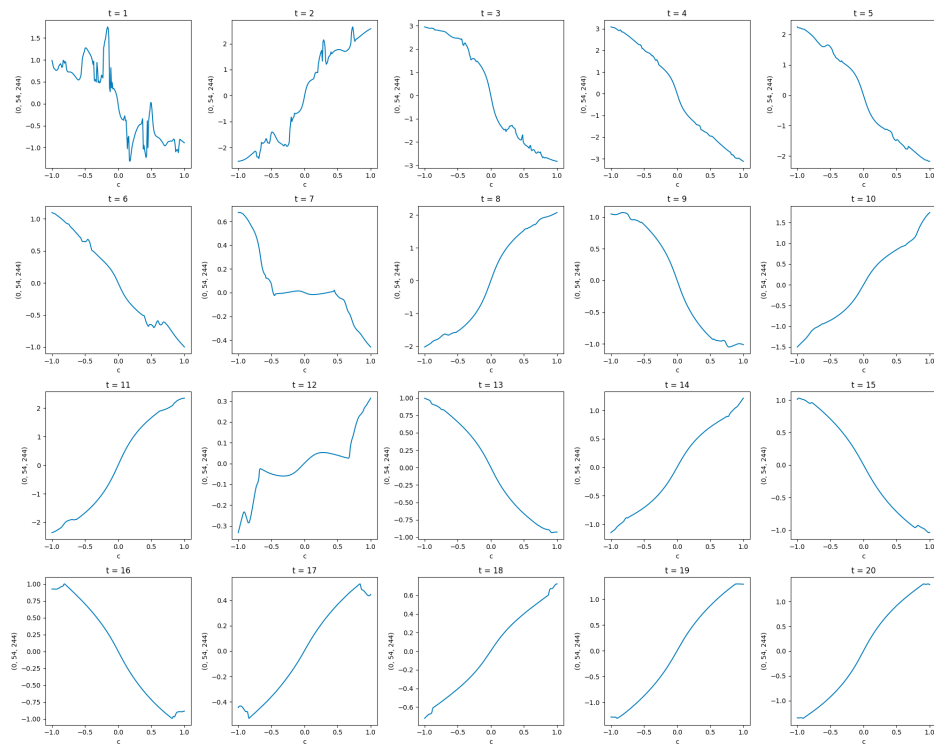


Figure 14: Church: Coordinate (0, 54, 244)

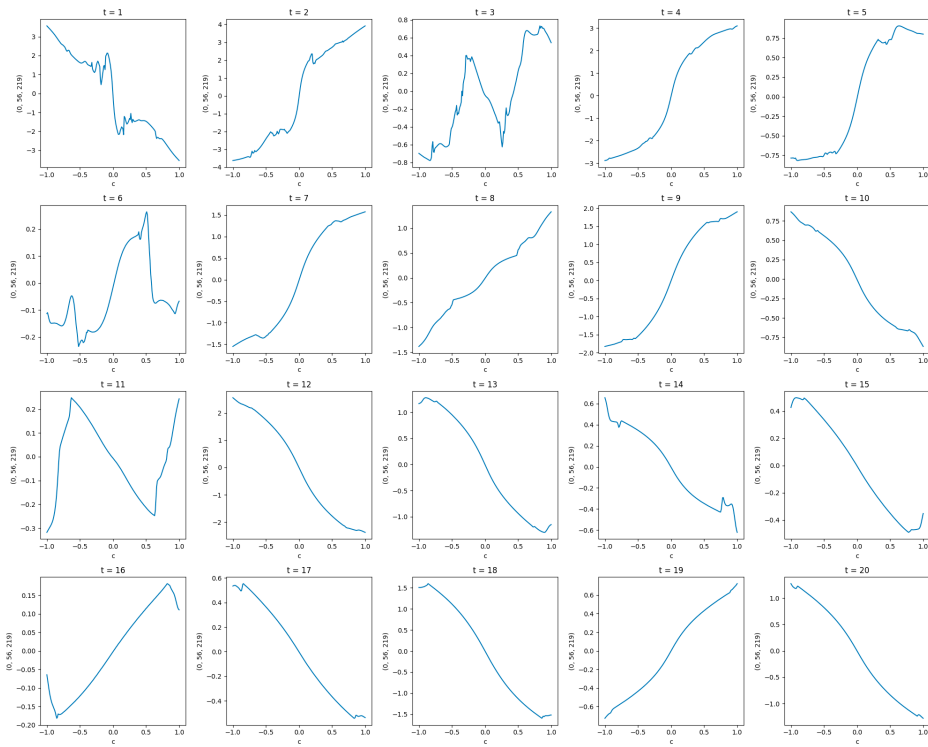


Figure 15: CIFAR10: Coordinate (0, 56, 219)

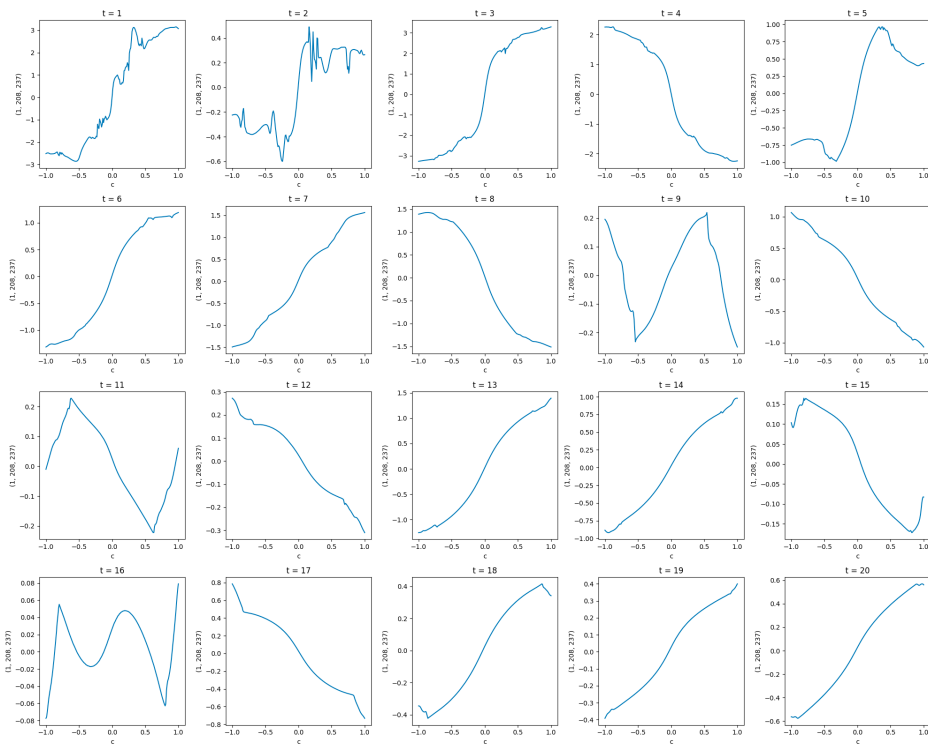


Figure 16: Church: Coordinate (1, 208, 237)

Table 7: Affine antisymmetry score

Dataset	CIFAR10	Church
Mean	0.9932	0.9909
Min	0.7733	0.7710
1% quantile	0.9104	0.8673
2% quantile	0.9444	0.8768
5% quantile	0.9690	0.9624
10% quantile	0.9865	0.9750
Median	0.9992	0.9995

## B.3 Additional experiments for uncertainty quantification

### B.3.1 Uncertainty Quantification

The image metrics used in uncertainty quantification are used to capture different aspects of pixel intensity, color distribution, and perceived brightness.

**Mean pixel value** is defined as the average of all pixel intensities across the image (including all channels). Formally, for an image  $I \in \mathbb{R}^{C \times H \times W}$ , the mean is computed as

$$\mu = \frac{1}{HWC} \sum_{i=1}^C \sum_{j=1}^H \sum_{k=1}^W I_{i,j,k}.$$

**Brightness** is calculated using the standard CIE formula:  $0.299 \cdot R + 0.587 \cdot G + 0.114 \cdot B$  to produce a grayscale value at *each pixel*, where  $R, G, B$  is the red, green, and blue color value of the given pixel. It is widely used in video and image compression, and approximates human visual sensitivity to color. The brightness of an image is then the average of the grayscale value across all pixels.

**Contrast** is computed as the difference in average pixel intensity between the top and bottom halves of an image. Let  $x \in [0, 1]^{C \times H \times W}$  be the normalized image, we define contrast as  $100 \cdot (\mu_{\text{top}} - \mu_{\text{bottom}})$ , where  $\mu_{\text{top}}$  and  $\mu_{\text{bottom}}$  are the average intensities over the top and bottom halves, respectively.

**Centroid** measures the coordinate of the brightness-weighted center of mass of the image. For scalar comparison, we focus on the vertical component of the centroid to assess spatial uncertainty. After converting to grayscale  $M \in \mathbb{R}^{H \times W}$  by averaging across channels, we treat the image as a 2D intensity distribution and compute the vertical centroid as

$$\frac{1}{\sum_{i=1}^H \sum_{j=1}^W M_{i,j}} \sum_{i=1}^H \sum_{j=1}^W i \cdot M_{i,j},$$

where  $i$  denotes the row index.

### B.3.2 QMC Experiments

**RQMC confidence interval construction:** For the RQMC experiments, we consider  $R$  independent randomization of a Sobol' point set of size  $n$ , with a fixed budget of  $N = Rn$  function evaluations. Denote the RQMC point set in the  $r$ -th replicate as  $\{\mathbf{u}_{r,k}\}_{1 \leq k \leq n} \subset [0, 1]^d$ , where  $\mathbf{u}_{r,k} \sim \text{Unif}([0, 1]^d)$ . Applying the Gaussian inverse cumulative distribution function  $\Phi^{-1}$  to each coordinate of  $\mathbf{u}_{r,k}$  transforms the uniform samples to standard normal samples. Consequently, the estimate in each replicate is given by

$$\hat{\mu}_r^{\text{QMC}} = \frac{1}{n} \sum_{k=1}^n S(\text{DM}(\Phi^{-1}(\mathbf{u}_{r,k}))), \quad r = 1, \dots, R.$$

The overall point estimate is their average

$$\hat{\mu}_N^{\text{QMC}} = \frac{1}{R} \sum_{r=1}^R \hat{\mu}_r^{\text{QMC}}.$$

Let  $(\hat{\sigma}_R^{\text{QMC}})^2$  be the sample variance of  $\hat{\mu}_1^{\text{QMC}}, \dots, \hat{\mu}_R^{\text{QMC}}$ . The Student  $t$  confidence interval is given by

$$\text{CI}_N^{\text{QMC}}(1 - \alpha) = \hat{\mu}_N^{\text{QMC}} \pm t_{R-1, 1-\alpha/2} \frac{\hat{\sigma}_R^{\text{QMC}}}{\sqrt{R}},$$

where  $t_{R-1, 1-\alpha/2}$  is the  $(1 - \alpha/2)$ -quantile of the  $t$ -distribution with  $R - 1$  degrees of freedom. If the estimates  $\hat{\mu}_r^{\text{QMC}}$  are normally distributed, this confidence interval has exact coverage probability  $1 - \alpha$ . In general, the validity of Student  $t$  confidence interval is justified by CLT. An extensive numerical study by [29] demonstrates that Student  $t$  intervals achieve the desired coverage empirically.

**Exploring different configurations of  $R$  and  $n$**  This experiment aims to understand how different configurations of  $R$ , the number of replicates, and  $n$ , the size of the QMC point set, affect the CI length of the RQMC method. The total budget of function evaluations is fixed at  $Rn = 3200$ , to be consistent with the AMC and MC experiments. We consider the four image metrics used in Section 4 and one additional image metric, MUSIQ.

For RQMC, each configuration was repeated five times, and the results were averaged to ensure stability. AMC and MC each consist of a single run over 3200 images. All experiments are conducted using the CIFAR10 dataset.

The results are shown in Table 8 and underlined values indicate the best CI length among the three QMC configurations, while bold values indicate the best CI length across all methods, including MC and AMC. For the brightness and pixel mean metrics, the configuration with point set size  $n = 64$  and number of replicates  $R = 50$  reduces CI

length the most. In contrast and centroid, the configuration with larger  $n$  has a better CI length. For MUSIQ, a more complex metric, changes in CI lengths across configurations are subtle, and the configuration with the largest  $R$  has the shortest CI length. While no single configuration consistently advantages, all RQMC and antithetic sampling methods outperform plain MC.

Table 8: Average 95% CI length and relative efficiencies (vs MC baseline). The first three rows are for RQMC methods, with the configuration of  $R \times n$  indicated in the first column.

$R \times n$	<b>Brightness</b>		<b>Mean</b>		<b>Contrast</b>		<b>Centroid</b>		<b>MUSIQ</b>	
	CI	Eff.	CI	Eff.	CI	Eff.	CI	Eff.	CI	Eff.
$25 \times 128$	0.37	29.81	0.40	25.71	<b>0.22</b>	<b>24.57</b>	<b>0.04</b>	<b>8.17</b>	0.13	1.11
$50 \times 64$	<u>0.35</u>	<u>32.05</u>	<u>0.39</u>	<u>26.94</u>	0.22	23.43	0.04	7.35	0.13	1.13
$200 \times 16$	0.47	18.38	0.49	17.30	0.29	14.20	0.05	5.84	<b>0.12</b>	<b>1.21</b>
AMC	<b>0.35</b>	<b>32.66</b>	<b>0.39</b>	<b>27.12</b>	0.23	22.05	0.04	6.96	0.13	1.06
MC	2.00	-	2.04	-	1.08	-	0.11	-	0.13	-

### B.3.3 DPS Experiment

We evaluate the confidence interval length reduction benefits of antithetic initial noise across four common image inverse problems: super-resolution, motion deblurring, Gaussian deblurring, and inpainting. For each task, the forward measurement operator is applied to the true image, and noisy observations are generated using Gaussian noise with  $\sigma = 0.05$ . We use the official implementation of DPS [7] with the following parameters:

- **Super-resolution** uses the *super\_resolution* operator with an input shape of (1, 3, 256, 256) and an upsampling scale factor of 2. This models the standard bicubic downsampling scenario followed by Gaussian noise corruption.
- **Motion deblurring** is configured using the *motion\_blur* operator with a kernel size of 61 and intensity of 0.1, which emulates motion-induced linear blur typical of camera shake, followed by additive noise.
- **Gaussian deblurring** employs the *gaussian\_blur* operator, again with a kernel size of 61 but with intensity set to 1, which is intended to test the variance reduction in a simpler inverse scenario.
- **Inpainting** is set up using the *inpainting* operator with a random binary mask applied to the input image. The missing pixel ratio is drawn from a uniform range between 30% and 70%, and the image size is fixed at  $256 \times 256$ . A higher guidance scale (0.5) is used to compensate for the sparsity of observed pixels.

As shown in Table 9, AMC consistently achieves shorter CI lengths than MC across all tasks and metrics without sacrificing reconstruction quality, implied by the L1 and PSNR metrics to measure the difference between reconstructed images and ground truth images.

Table 9: Comparison of AMC vs. MC across tasks in DPS

Task	Metric	Group	Mean	CI Length	Effi.
Motion Deblur	L1	AMC	24.6878	<b>1.1615</b>	1.0342
		MC	24.5166	1.1833	
	PSNR	AMC	17.9595	<b>0.3012</b>	1.1222
		MC	18.0234	0.3380	
Super-resolution	L1	AMC	28.1603	<b>1.0115</b>	1.4075
		MC	28.1357	1.2000	
	PSNR	AMC	16.8561	<b>0.2592</b>	1.2045
		MC	16.8644	0.3122	
Gaussian Deblur	L1	AMC	22.6941	<b>0.8879</b>	1.3113
		MC	22.6600	1.0171	
	PSNR	AMC	18.6994	<b>0.2651</b>	1.4364
		MC	18.7102	0.3179	
Inpainting	L1	AMC	21.8591	<b>0.8286</b>	1.5388
		MC	21.9821	1.0279	
	PSNR	AMC	19.0290	<b>0.2575</b>	1.7066
		MC	18.9807	0.3364	

## C More visualizations

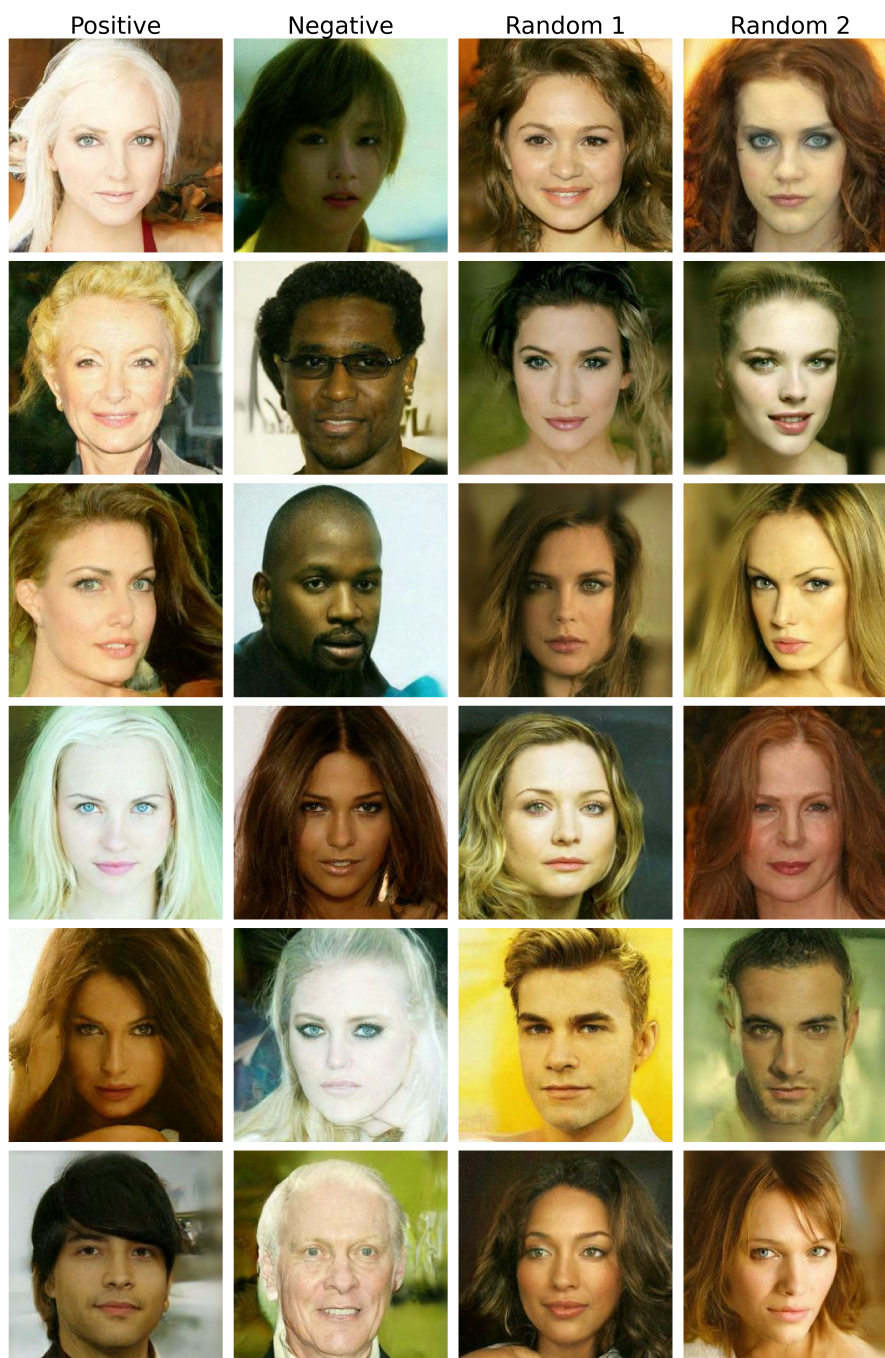


Figure 17: CelebA-HQ Image Generated

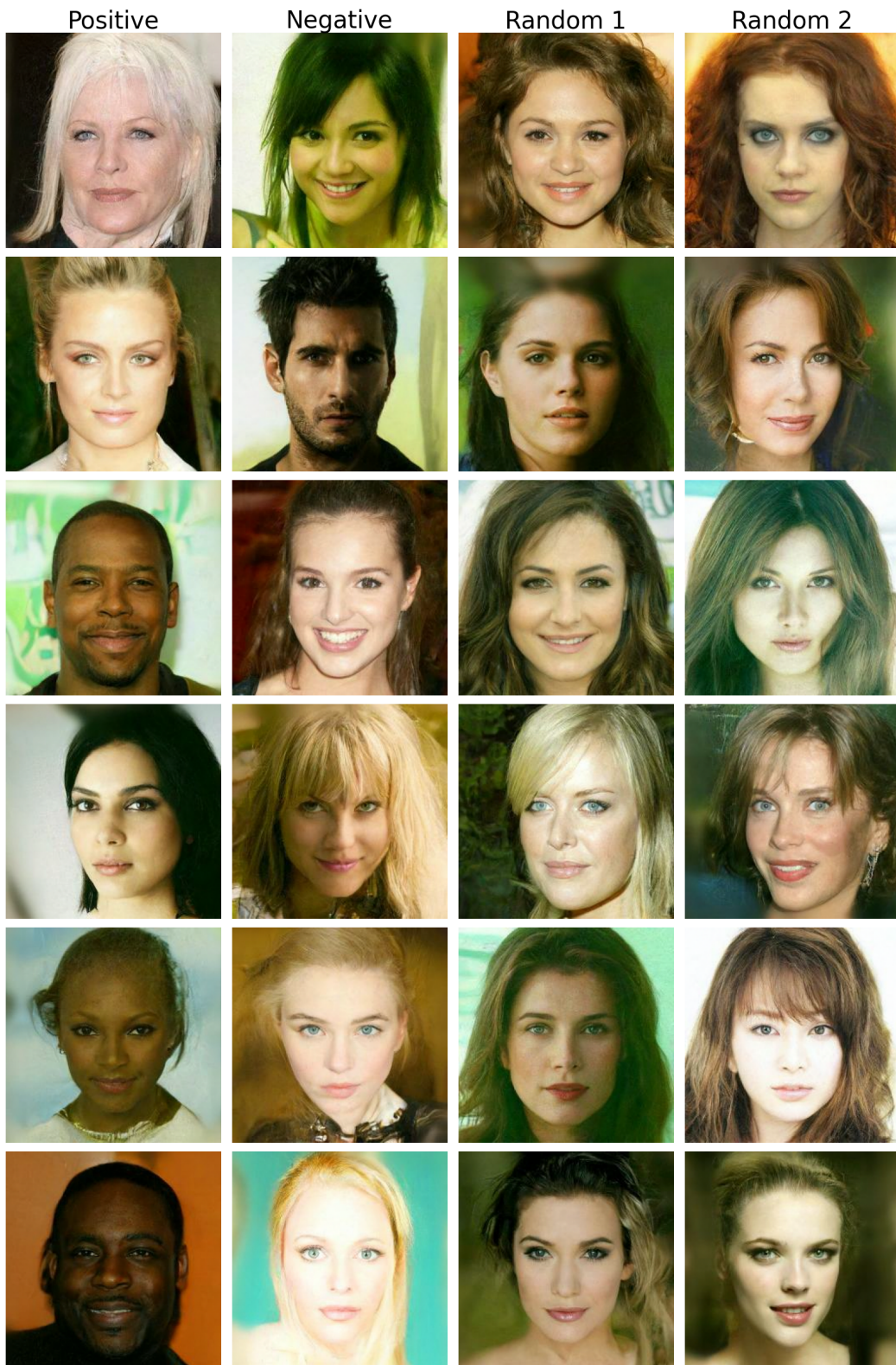


Figure 18: CelebA-HQ Image Generated

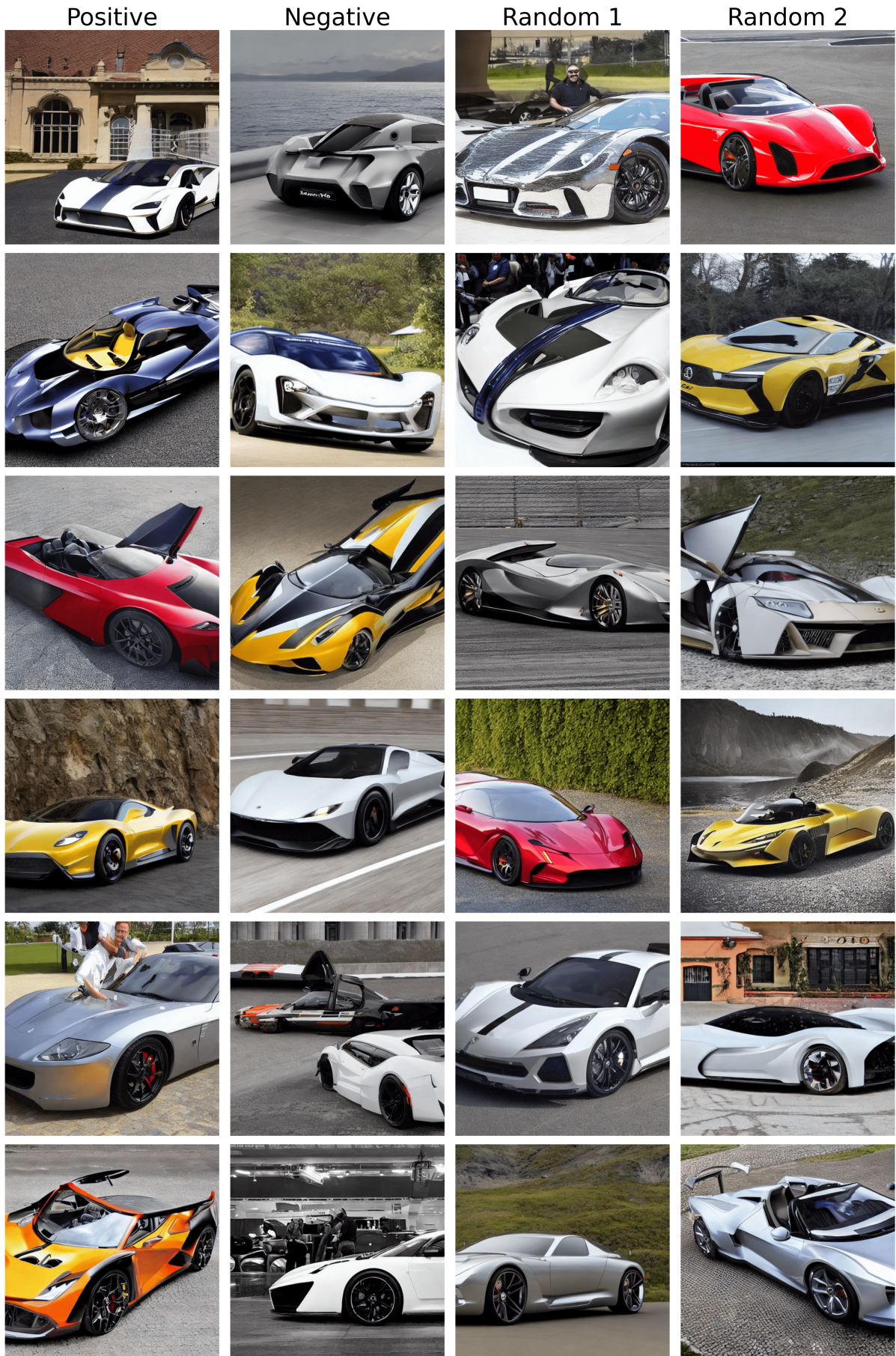


Figure 19: Prompt: "most expensive sports car"



Figure 20: Prompt: "little bunny"